nature COMMUNICATIONS

ARTICLE

Received 7 Aug 2015 | Accepted 3 Feb 2016 | Published 24 Mar 2016

DOI: 10.1038/ncomms10952 OPEN

Understanding silicate hydration from quantitative analyses of hydrating tricalcium silicates

Elizaveta Pustovgar[1], Rahul P. Sangodkar[2], Andrey S. Andreev[3], Marta Palacios[1], Bradley F. Chmelka[2], Robert J. Flatt[1] & Jean-Baptiste d'Espinose de Lacaillerie[1,3]

Silicate hydration is prevalent in natural and technological processes, such as, mineral weathering, glass alteration, zeolite syntheses and cement hydration. Tricalcium silicate (Ca_3SiO_5), the main constituent of Portland cement, is amongst the most reactive silicates in water. Despite its widespread industrial use, the reaction of Ca_3SiO_5 with water to form calcium-silicate-hydrates (C-S-H) still hosts many open questions. Here, we show that solid-state nuclear magnetic resonance measurements of ^{29}Si-enriched triclinic Ca_3SiO_5 enable the quantitative monitoring of the hydration process in terms of transient local molecular composition, extent of silicate hydration and polymerization. This provides insights on the relative influence of surface hydroxylation and hydrate precipitation on the hydration rate. When the rate drops, the amount of hydroxylated Ca_3SiO_5 decreases, thus demonstrating the partial passivation of the surface during the deceleration stage. Moreover, the relative quantities of monomers, dimers, pentamers and octamers in the C-S-H structure are measured.

[1] Institute for Building Materials, Department of Civil, Environmental and Geomatic Engineering, ETH Zürich 8093, Switzerland. [2] Department of Chemical Engineering, University of California, Santa Barbara, California 93106, USA. [3] Soft Matter Science and Engineering Laboratory, UMR CNRS 7615, ESPCI Paris, PSL Research University, 10 rue Vauquelin, Paris 75005, France. Correspondence and requests for materials should be addressed to J.-B.d.E.d.L. (email: jean-baptiste.despinose@espci.fr).

Since Le Chatelier[1], it is well understood that Portland cement hydration is initiated by the dissolution of calcium silicate monomers in water, followed by the precipitation of less soluble layered calcium-silicate-hydrates (C-S-H), in which silicate ions condense to form short chains. However, despite two centuries of widespread applications and a century of detailed study, the molecular mechanisms behind the kinetic stages of hydration (that is, induction, acceleration and deceleration) are still debated. Similar kinetic stages are observed in various heterogeneous hydration processes occurring during mineral weathering[2,3], glass alteration[4,5] and hydrothermal syntheses. For example, although hydrothermal zeolite syntheses under alkaline aqueous conditions proceeds over different timescales[6], the effective reaction rates in cementitious and zeolite systems exhibit similar distinct stages (induction, acceleration and deceleration), and are governed by several coupled parameters varying in space and time near the liquid–solid interface. This situation is thus extremely complex to describe accurately. An added difficulty is that for porous materials such as cement or zeolites, interfacial energy contributes to the stabilization of nanoscale intermediates, which are typically challenging to characterize. For Portland cement in particular, the lack of quantitative experimental data obtained with sufficient time resolution has precluded the validation of existing models aimed at explaining the complex kinetics of cement hydration.

Similar to the homogeneous versus heterogeneous pathways dichotomy in zeolite crystallization mechanisms[7], two landmark competing theories have been proposed to explain the early-age time dependence of the rate of tricalcium silicate (Ca_3SiO_5) hydration, the principal component in commercial Portland cements responsible for the development of mechanical strength[8–10]. The first theory proposes that early-age hydration products form a diffusion barrier on the surfaces of Ca_3SiO_5 particles, thus affecting subsequent reactions of the underlying non-hydrated core[11]. The second theory[12–14] suggests that the early-age time-dependence of the rate of hydration is determined by the rate of Ca_3SiO_5 dissolution and by a change in the associated rate limiting step from etch pit formation to step retreat, which is a mechanism also often invoked in the geochemical literature on natural weathering[15,16]. The relevance of these theories to silicate hydration can be examined by understanding the molecular compositions and structures of species at the solid–liquid interfaces during the early stages of hydration. Similar questions are raised in heterogeneous catalysis and geochemistry; however, Portland cement hydration faces the additional complexity that the main product, C-S-H, is not only poorly crystalline but also nanostructured with variable stoichiometry and silicate coordinations[17,18]. These challenges have been previously addressed partially through numerical modelling of hydration reactions at Ca_3SiO_5 surfaces[19,20] and of the local structure and disorder of the resulting hydration products[21]. Nevertheless, these models suffer from a lack of experimental support at the molecular level.

Here, solid-state NMR measurements of triclinic ^{29}Si-enriched Ca_3SiO_5 hydration are used to determine the transient molecular-level compositions at silicate surfaces and the interactions between silicate species, hydroxyl groups and water molecules, which influence the rates of hydration reactions. The isotopic ^{29}Si enrichment provides significantly enhanced NMR signal sensitivity that can be used to monitor the structures of the hydrates *in situ* during the hydration process, as a function of hydration time. In addition, ^{29}Si enrichment enabled two-dimensional (2D) through-bond (*J*-mediated) NMR measurements that are sensitive to ^{29}Si-O-^{29}Si covalent bonding. They are used to crucially provide detailed information on the local atomic-level compositions, structures and site connectivities in hydrated silicate species, here C-S-H. These analyses shed new insights on the origin of rate limiting steps and the kinetics of silicate polymerization at the solid–liquid interface during Ca_3SiO_5 hydration.

Results

Experimental approach. To the seminal approach of ^{29}Si enrichment by Brough *et al.*[22], we added for the first time the sophistication of carefully controlled structure and granulometry of the Ca_3SiO_5 particles (see Supplementary Methods) and hydration reaction conditions (see Supplementary Notes 1 and 2). Indeed the surface structure and area of the Ca_3SiO_5 particles strongly affect their reactivity, which must be carefully controlled to ensure meaningful results[23]. For example, the high surface area of the synthesized ^{29}Si-enriched Ca_3SiO_5 ($4.4\,m^2\,g^{-1}$, see Supplementary Methods) allowed ~90% of the silicate hydration process to be monitored in 24 h of NMR spectrometer time, without external acceleration. In this way, subtle and unique quantitative information pertinent to hydration mechanisms can be obtained non-invasively and with a time resolution of 30 min

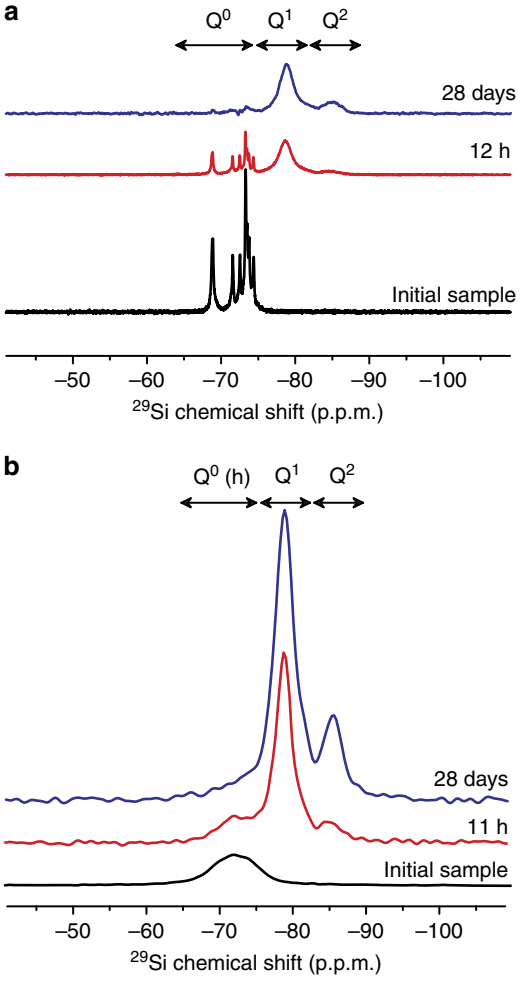

Figure 1 | Dynamics of silicate hydrates formation studied *in situ* by ^{29}Si NMR. (**a**) ^{29}Si MAS NMR and (**b**) $\{^1H\}^{29}$Si CPMAS NMR spectra of ^{29}Si-enriched triclinic Ca_3SiO_5 sample in its initial non-hydrated state (in black) and after hydration for 11 or 12 h (in red) and 28 days (in blue). ^{29}Si resonances from isolated silicate (Q^0) species in non-hydrated Ca_3SiO_5, hydoxylated surface Q^0 (Q^0(h)) species and polymerized calcium-silicate-hydrates (Q^1 and Q^2) are clearly resolved and can be quantified as a function of time.

(measurement time for the NMR spectra). Consequently, the progress of the hydration reaction could be accurately and quantitatively correlated to the corresponding ^{29}Si speciation. In addition, ^{29}Si enrichment allows NMR measurements to be performed on samples without the need for conventional water removal schemes for quenching the hydration process[24], which otherwise often disrupt the fragile microstructure of the C-S-H or may detrimentally alter chemical composition. Representative one-pulse ^{29}Si and ^{1}H{^{29}Si} cross-polarization (CP) magic-angle-spinning (MAS) NMR spectra are presented in Fig. 1a,b, respectively, for non-hydrated and hydrated Ca_3SiO_5. In anhydrous triclinic Ca_3SiO_5 which exhibits long-range crystalline order and well-defined local atomic ^{29}Si environments, eight distinct and narrow (<0.5 p.p.m. full-width at half maximum (FWHM)) ^{29}Si signals are resolved between −68 and −75 p.p.m. corresponding to anhydrous Q^0 species (Supplementary Fig. 2). In contrast, in hydration products, the ^{29}Si resonances are broad (3–4 p.p.m. FWHM) with signals centred at −72, −79 and −85 p.p.m. from silanol Q^0(h), hydrated Q^1 and hydrated Q^2 silicate species, respectively (Fig. 1). The last two species are associated with the C-S-H structure (Q^n refers to silicon atoms that are covalently bonded via bridging oxygen atoms to $0 \le n \le 4$ other silicon atoms[25]). These molecular-level insights of the local silicate structures in Ca_3SiO_5 hydration products (C-S-H) are consistent with previous ^{29}Si NMR (refs 26,27), ^{17}O NMR (ref. 28), X-ray and neutron scattering results[18] for C-S-H.

The degree of silicate hydration is determined by quantitative *in situ* ^{29}Si NMR analyses and forms the crux of our results, which are summarized in Fig. 2. These results are in close agreement with the degree of silicate hydration as established by independent isothermal calorimetric measurements, which reveal the successive stages of initial dissolution, induction, acceleration and deceleration (Fig. 2b) during the silicate hydration process. This comparison crucially establishes the accuracy of the quantitative ^{29}Si NMR results acquired during Ca_3SiO_5 hydration, and indicates that the hydration process is negligibly altered by factors such as the MAS conditions of the NMR experiment (see Supplementary Notes 1 and 2). This detailed time-resolved, *in situ*, quantitative NMR analysis answers three central questions about Ca_3SiO_5 hydration: the molecular origin of the reduced apparent solubility of Ca_3SiO_5 during the induction period, the possible 'switch' from one type of hydration products to another between the acceleration and deceleration period, and the relative proportions of silica oligomers in the final C-S-H structure.

Induction period. The apparent solubility of Ca_3SiO_5 during the induction period of hydration has been reported to be lower compared with pristine anhydrous Ca_3SiO_5 (refs 11–13). This reduced apparent solubility has been proposed to arise from the deposition of a layer of hydration products (the metastable barrier hypothesis)[11] or from surface hydroxylation[12,13]. The molecular compositions at the Ca_3SiO_5 surface during this induction period

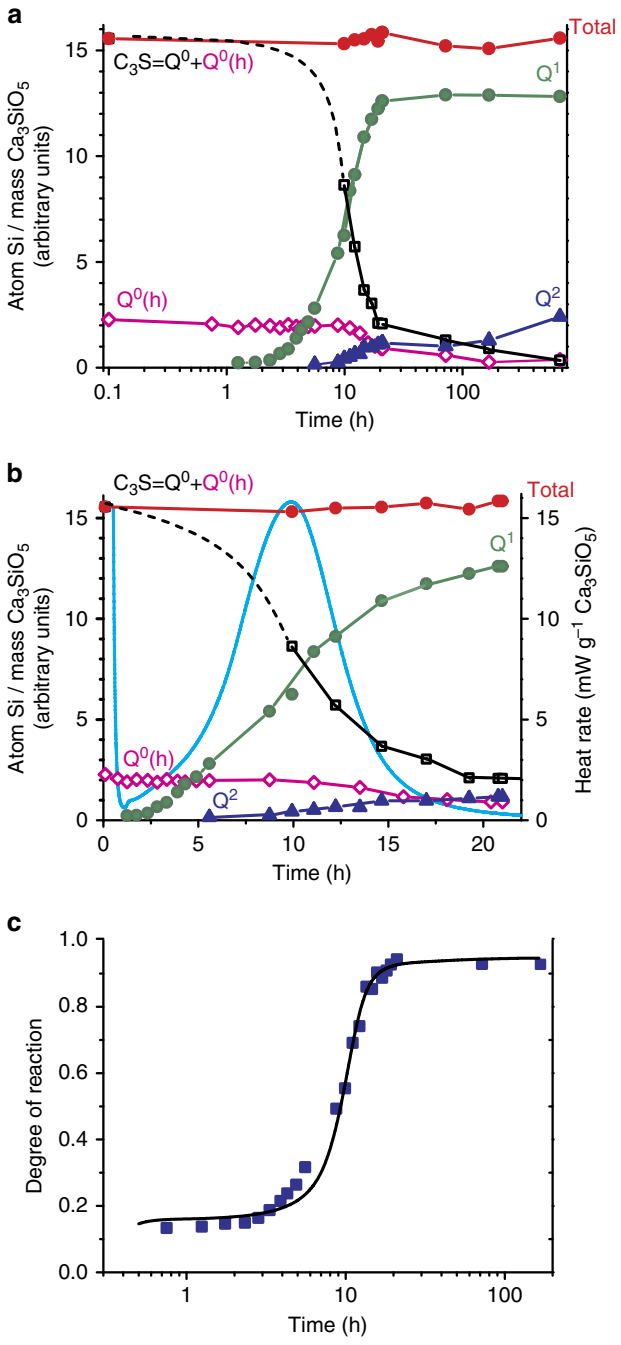

Figure 2 | Quantitative monitoring of silicate speciation during the hydration of ^{29}Si-enriched triclinic Ca_3SiO_5. (**a**) The quantities of different ^{29}Si silicate species as established by ^{29}Si MAS and {^{1}H}^{29}Si CPMAS NMR measurements for hydration times up to 28 days (see Supplementary Note 1). The quantities, normalized to the initial amount of Ca_3SiO_5, of anhydrous Q^0 (in black), hydroxylated Q^0(h) (in pink), hydrated Q^1 (in green), hydrated Q^2 (in blue) and total silicate species (in red) resulting from this analysis are as shown. (**b**) Comparison of the quantities of different ^{29}Si silicate species and the reaction heat flow rate determined by isothermal calorimetry (cyan line) for Ca_3SiO_5 up to 24 h of hydration. Based on the heat released in the calorimetry measurements, four stages in the hydration process can be identified: first a brief exothermic peak during the first few minutes (<15 min) corresponding to initial dissolution of Ca_3SiO_5, then a short (15 min–2 h) induction period during which no significant heat is released, followed by a peak corresponding to the acceleration period (2–10 h), and finally the deceleration period (>10 h) associated with decreasing rate of heat release (Supplementary Fig. 8). (**c**) Comparison of the degree of silicate hydration determined independently by ^{29}Si MAS and {^{1}H}^{29}Si CPMAS NMR quantitative analyses (squares) and isothermal calorimetry results (black line), which are in close agreement. The fact that the total amount of Si atoms remains constant, within the uncertainties of the measurements, over the entire hydration period (28 days) establishes the accuracy of the associated quantitative NMR methods and analyses. Details of these analyses are included in the Supplementary Note 1.

(as determined by the NMR analyses presented here) points towards the latter scenario. The $^{29}Si\{^{1}H\}$ CPMAS NMR measurements of the initial sample (that is, non-hydrated) (Fig. 1b) establish the presence of Q^0 silicate species in proximity to protons (henceforth labelled $Q^0(h)$) on Ca_3SiO_5 particle surfaces, even before contact with bulk water. Although previous studies have reported the presence of similar $Q^0(h)$ silicate species at the surfaces of 'anhydrous' Ca_3SiO_5 particles[22,26], it has not been largely publicized nor quantitatively analysed. The 2D $^{29}Si\{^{1}H\}$ heteronuclear correlation (HETCOR) NMR spectrum of the same sample of non-hydrated Ca_3SiO_5 (Fig. 3) exhibits correlated intensities between the ^{29}Si signal at -72 p.p.m. from $Q^0(h)$ species and unresolved ^{1}H signals around 1.3 and 0.9 p.p.m. from –SiOH and -CaOH moieties, thereby establishing the close molecular-level proximities of surface $Q^0(h)$ species to at least one type of such ^{1}H moieties. In addition, the absence of resonances characteristic of polymerized hydration products (that is, Q^1 and Q^2 species), establishes that the reaction of surface silicate species in non-hydrated Ca_3SiO_5 with atmospheric moisture results solely in the formation of hydroxylated $Q^0(h)$ species at particle surfaces, within the sensitivity limits of the measurement. In other words, no separate hydrate phase forms at this stage, it is solely the Ca_3SiO_5 particle near-surface which is hydroxylated.

From a crystal chemistry perspective, the Ca_3SiO_5 particle surface is unlikely to be inert when exposed to atmospheric water vapour. Specifically, Ca_3SiO_5 is an ionic crystal of Ca^{2+} cations with oxide and monomeric silicate anions ($3Ca^{2+} \cdot O^{2-} \cdot SiO_4{}^{4-}$) (refs 19,29). There is a strong ionization of the atoms ($+1.5$ on Ca^{2+} and -1.5 on O^{2-}) (ref. 19) and consequently Ca_3SiO_5 acts as a basic oxide that readily yields hydroxide ions when reacting with water,

$$O^{2} + H_2O \rightarrow 2\,OH^{-} \qquad (1)$$

Therefore, one expects OH^- to replace oxide ions on the particle surfaces. However, replacement of one O^{2-} by two OH^- would yield a heterogeneous distribution of local atomic environments at the Ca_3SiO_5 surface, due to the different sizes and formal charges of these anions. Indeed the $Q^0(h)$ ^{29}Si NMR resonance of the initial sample is very broad (Fig. 1b), reflecting a wide distribution of local ^{29}Si environments. In summary, the ^{29}Si NMR analyses reveal that near-surface ^{29}Si species on Ca_3SiO_5 particles are predominantly hydroxylated and that negligible quantities of polymerized silicate hydration products form (within the sensitive detection limits of the measurements), a result consistent with previous force-field atomistic simulations[19]. Overall, hydroxylated Q^0 (h) species are predominant at particle surfaces during the induction period and expected to result in the reduced apparent solubility of Ca_3SiO_5, compared with pristine anhydrous Ca_3SiO_5 whose level of hydroxylation is lower.

Acceleration stage. With the progress of Ca_3SiO_5 hydration, the monomeric Q^0 silicate species polymerize to form oligomeric units of C-S-H. As shown in Fig. 2, while the population of hydroxylated $Q^0(h)$ species remains constant, the populations of Q^1 species increase significantly during the acceleration stage ($\sim$2–10 h). Compared with the induction stage ($<$2 h), the ^{29}Si polymerization during the acceleration stage results predominantly in the formation of Q^1 species (dimers) at early times, and a combination of Q^1 and Q^2 species (for example, pentamers and octamers) at later time (10–20 h). In particular, the population of Q^1 species increases approximately linearly with the progress of hydration (Fig. 2b) across the entire acceleration stage, consistent with the formation of predominantly dimeric C-S-H units. No significant change nor in the silicon second coordination sphere of the hydration products nor in their rate of formation could be detected at this stage.

Deceleration stage. The data in Fig. 2 indicate that at the end of the acceleration stage (after $\sim$10 h in the present case) greater quantities of long ($>$2 silicate tetrahedra) C-S-H chains containing Q^2 species are formed compared with dimeric C-S-H units (without Q^2). Although the amounts of Q^2 species increase progressively after the hydration peak ($\sim$20 h), the population of Q^1 species remains approximately constant, which indicates the formation of longer silicate chains besides the dimers. By comparison, the amount of $Q^0(h)$ species remains constant for several hours ($\sim$10 h) during the induction and acceleration stages, it subsequently decreases just when, according to isothermal calorimetry, the Ca_3SiO_5 hydration slows down, that is during the so-called deceleration stage. This observation provides

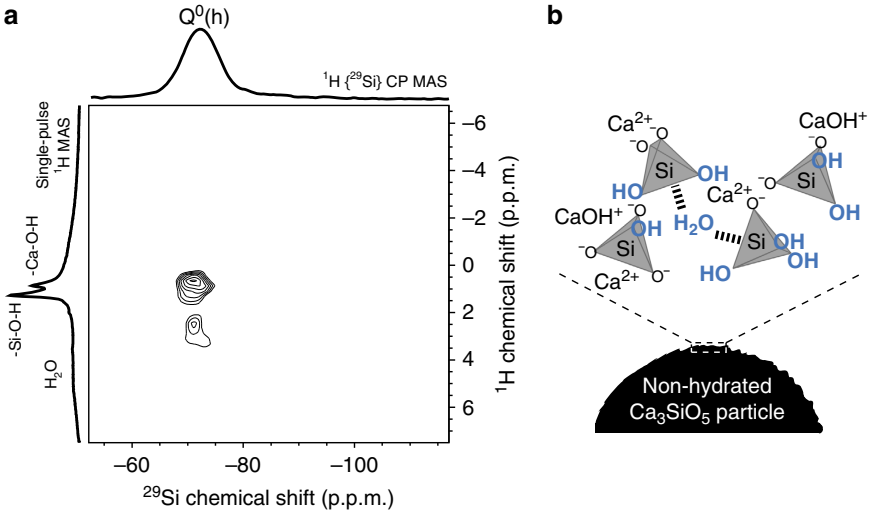

Figure 3 | Proton to silicon signal intensity correlations on the initial non-hydrated ^{29}Si-enriched triclinic Ca_3SiO_5. (**a**) The 2D $\{^{1}H\}$ ^{29}Si HETCOR NMR spectrum shows intensity correlations between ^{29}Si and ^{1}H signals that result from molecular proximity between ^{29}Si and ^{1}H nuclei. ^{29}Si CPMAS and ^{1}H MAS 1D spectra are shown along the horizontal and vertical axis of the 2D spectrum. The chemical shift of ^{29}Si is detected (horizontal dimension), while chemical shift of ^{1}H is recorded in the indirect (vertical) dimension. (**b**) The right inset schematizes the protonated moieties detected on the Ca_3SiO_5 surfaces.

important insights regarding the debate on the origin of the deceleration period. While some previous studies suggest that the deceleration period results from coverage of Ca_3SiO_5 particles by hydration products[30], others claim that hydration initially results in products forming a low-density structure, the subsequent densification of which corresponds to the beginning of the deceleration stage[31,32]. Our analyses suggest that compared with the acceleration period that is associated with the formation of predominantly dimeric C-S-H units, the deceleration period corresponds to the formation of greater relative fractions of C-S-H units with longer chain lengths. Such increasing extents of silicate polymerization might possibly be accompanied by an increased density of the C-S-H that consequently would present a diffusion barrier for mass transport and, thus, slow the rate of hydration reaction, consistent with the deceleration stage. This alone is not conclusive as it could either support the view according to which the deceleration would be based indeed on the filling of an ultra-low-density gel[33] or the one based on an inhibition of hydration by hydrates themselves[34], impinging on each other's growth[35,36]. Nevertheless, the decrease of the amount of near-surface Q^0(h) species population at the onset of the deceleration period reflects a proportional decrease of the average surface area available to drive hydration by silicate dissolution. The decrease of the particles surface area as revealed here by NMR supports strongly the conclusions of recent modelling studies[37], namely that the deceleration stage results from the reduction of the average particle surface area available for reaction due to increasing surface coverage of the Ca_3SiO_5 particles by hydration products. This conclusion is also supported by the fact that at 7 days 5% of the Ca_3SiO_5 has not yet hydrated, bringing support to a coverage and passivation of its surface by deposited hydrates. Moreover, the long period during which Q^0(h) remains constant suggests that during dissolution, the surface decrease due to the reduction in particle size is compensated by roughening (opening of etch pits and step retreat)[38]. In other words dissolution does not simply proceed by shrinking of the core of the particles, but also by etching.

Final C-S-H structure. The atomic site interconnectivities of different silicate species can be used to elucidate the molecular structures and lengths of silicate chains in the C-S-H. Such detailed insights can be obtained by using solid-state 2D *J*-mediated $^{29}Si\{^{29}Si\}$ correlation NMR techniques[39] that probe *J*-coupled ^{29}Si-O-^{29}Si spin pairs and have been previously applied to establish silicate framework connectivities in a variety of heterogeneous materials[40–43]. Previously, Brunet *et al.*[44] have conducted 2D dipolar-mediated $^{29}Si\{^{29}Si\}$ NMR measurements that rely on through-space ^{29}Si-^{29}Si dipolar couplings and which yield information on the molecular-level proximities of different ^{29}Si moieties in synthetic C-S-H. However, such measurements cannot be used to directly establish the covalent connectivity among different ^{29}Si moieties in the C-S-H structure. In contrast, by relying on through-bond *J*-interactions associated with ^{29}Si-O-^{29}Si moieties (*J*-interactions between ^{29}Si spin pairs separated by more than two covalent bonds are negligibly small and consequently expected to be below the detection limits of the 2D *J*-mediated $^{29}Si\{^{29}Si\}$ NMR measurement.), 2D *J*-mediated $^{29}Si\{^{29}Si\}$ double-quantum (DQ) correlation NMR measurements provide detailed insights regarding the tetrahedral site connectivity in the C-S-H chains. Notably, the 2D *J*-mediated $^{29}Si\{^{29}Si\}$ NMR spectrum of hydrated ^{29}Si-labelled Ca_3SiO_5 shown in Fig. 4b provides significantly enhanced ^{29}Si resolution, compared with the single-pulse ^{29}Si MAS spectrum (Fig. 4a), and unambiguously establishes distinct ^{29}Si-O-^{29}Si covalent connectivities in the silicate chains.

The 2D *J*-mediated $^{29}Si\{^{29}Si\}$ NMR spectrum (Fig. 4b) exhibits three well separated regions of correlated intensities in the Q^1 (approximately -79 p.p.m.) and Q^2 (approximately -85 p.p.m.) chemical shift ranges along the single-quantum (SQ)–DQ $y=2x$ line, and two pairs of cross-correlated peaks between the Q^1 and Q^2 chemical shifts ranges. The broad continuous distribution of correlated chemical shifts in the 2D $^{29}Si\{^{29}Si\}$ spectrum between signals at -82 and -87 p.p.m. in the ^{29}Si SQ dimension are attributed to different ^{29}Si-O-^{29}Si Q^2 moieties, consistent with the structural disorder of C-S-H. Interestingly, the spectrum reveals narrow (0.6 p.p.m. FWHM) ridges of intensity correlations that are parallel to the SQ–DQ line. Such features typically arise from structural disorder on length scales (>1 nm) that are larger than the distances between the ^{29}Si-^{29}Si spin pairs (or also due to anisotropy in the magnetic susceptibility)[45]. The presence of such poor long-range structural order is consistent with the broad distributions of local ^{29}Si environments that are associated with the heterogeneous nature of the C-S-H. Nevertheless, careful analysis of the 2D spectrum distinguishes discrete correlated signal intensities that are resolved to greater than a tenth of a p.p.m. Specifically, a strong correlated intensity (labelled *i*) between the ^{29}Si signals centred at -84.8 and -85.4 p.p.m. in the SQ dimension and at -170.2 p.p.m. in the DQ dimension (Supplementary Fig. 11) unambiguously establishes the presence of two chemically distinct Q^2 ^{29}Si species that are covalently bonded through a shared bridging oxygen atom. The different isotropic ^{29}Si chemical shifts of these distinct Q^2 species likely reflect differences in the number and types of species in the C-S-H interlayer (calcium ions or proton moieties such OH groups or water molecules) that are in close (<1 nm) molecular-level proximity to the non-bridging oxygen atoms of the four-coordinate silicate units. Indeed, the different electronegativities of Ca^{2+} and H^+ result in different ^{29}Si nuclear shielding, as shown by recent density functional theory calculations[46]. These molecular-level differences in the Q^2 species are shown in the schematic diagram (Fig. 4, inset) of a postulated structure of C-S-H that is consistent with the observed 2D NMR correlations (as well as previous experimental[28,18] and modelling analyses[17,47]). Although the Q^{2L} resonances (the four-coordinate Q^2 silicate units that are positioned away from the interlayer space between two C-S-H chains, as shown in the inset in Fig. 4) are not resolved in the spectrum, the external ridges of the Q^2 correlation spot correspond to correlated intensity between the ^{29}Si SQ signals of the two Q^2 silicate species at -85.4 and -84.8 p.p.m. with the ^{29}Si SQ signals from the Q^{2L} species to which they are, respectively, bound. Within this hypothesis and with the constraint that the DQ frequency must be the sum of the SQ frequencies, two additional correlations can be identified for the Q^2 species at SQ signals -85.4 and -84.8 p.p.m. at DQ signals approximately -168.9 p.p.m. (*ii*) and -168.1 p.p.m. (*iii*), respectively, thus establishing the presence of two distinct Q^{2L} species with SQ signals at -83.5 and -83.1 p.p.m. Furthermore, the same ^{29}Si SQ signals at -85.4 and -84.8 p.p.m. from the two Q^2 silicate species are also separately correlated with ^{29}Si signals centred around -79 p.p.m. (*iv*, *v*) (DQ $\simeq -164$ p.p.m.) from Q^1 species, further corroborating that these Q^2 species are indeed chemically distinct. Therefore, analyses of the 2D *J*-mediated $^{29}Si\{^{29}Si\}$ spectrum establish the occurrence of oligomeric silicate units with two distinct Q^2 and two distinct Q^{2L} species in the C-S-H structure.

The partially resolved pair correlated intensities (*ix*–*xii*) in the range of -77 to -80 p.p.m. reveal the presence of different types of Q^1 silicate species associated with at least four distinct dimeric C-S-H units. These results are further corroborated by differences in the spin–spin (T_2) relaxation-time behaviours of the associated ^{29}Si Q^1 species, which were exploited to provide

improved ^{29}Si resolution by using one-dimensional (1D) T_2-filtered ^{29}Si MAS measurements (Supplementary Fig. 12). In combination, the different pair correlated intensities establish the presence of dimeric units (*ix–xii*) and C-S-H chains that consist of two distinct Q^1-Q^2 (*iv*, *v*) and Q^2-Q^{2L} (*ii*, *iii*) connectivities and at least one Q^2-Q^2 (*i*) connectivity. To accommodate this diversity of atomic connectivity revealed by the 2D ^{29}Si{^{29}Si} NMR measurements, the C-S-H structure must contain a linear chain of at least eight four-coordinated silicate units (that is, an octamer). A similar analysis of pair correlated intensities *vi–viii* indicate the presence of pentameric C-S-H units, as discussed in the Supplementary Note 4. This result is supported by recent studies using density functional theory that have evaluated the relative stabilities of linear C-S-H units of different chain lengths and proposed the presence of stable octameric units[48], for which no direct experimental evidence has previously been available.

The relative populations of ^{29}Si silicate species associated with C-S-H units of different chain lengths (for example, dimers and octamers) are determined based on the enhanced ^{29}Si resolution afforded by the 2D ^{29}Si{^{29}Si} NMR spectrum. Specifically, the single-pulse ^{29}Si MAS spectrum shown in Fig. 5a can be simulated by using the peak positions of ^{29}Si signals as established by the 2D ^{29}Si{^{29}Si} NMR spectrum and the relative fractions of Q^1, Q^2 and Q^{2L} species associated with C-S-H units of different chain lengths (for example, $Q^2/Q^1 = 2$, $Q^2/Q^{2L} = 2$ for octamer as shown in Fig. 5b). Such an analysis yields estimates of 44, 7 and 42% (± 4%) for the relative populations of ^{29}Si silicate engaged in octameric, pentameric and dimeric units, respectively. These values correspond to 20 mole% octamers, 5 mole% pentamers and 75 mole% dimers in the C-S-H. The salient result is, thus, that despite the fact that the average chain length is 5, pentamers are actually a minority feature. Such distributions of chain lengths are consistent with previous studies that have reported mean chain lengths for C-S-H, which suggest the presence of pentamers and octamers, in addition to dimers[22,49–51]. It must be understood that the high amount of octamers was obtained here in a relatively short hydration times (1.5 month) compared with what would be required in a usual cement paste. Specifically, the use of pure tricalcium silicate, the high surface area (4.4 $m^2\,g^{-1}$) of the non-hydrated sample and the water-to-solids ratio (0.8) used in this study are expected to result in relatively fast hydration kinetics and a faster precipitation of C-S-H. The end result is a higher extent of hydration and silicate cross-linking. Interestingly, the analysis also indicates that small quantities of monomeric ^{29}Si silicate species, such as hydroxylated Q^0(h) (5 ± 1%) and anhydrous Q^0 (2 ± 1%), are present even after hydration of Ca_3SiO_5 for 1.5 months at 25 °C. These monomers likely arise from remnants of surface hydroxylation of Ca_3SiO_5 particles or are components of the C-S-H structure, which is consistent with recent numerical modelling results[47].

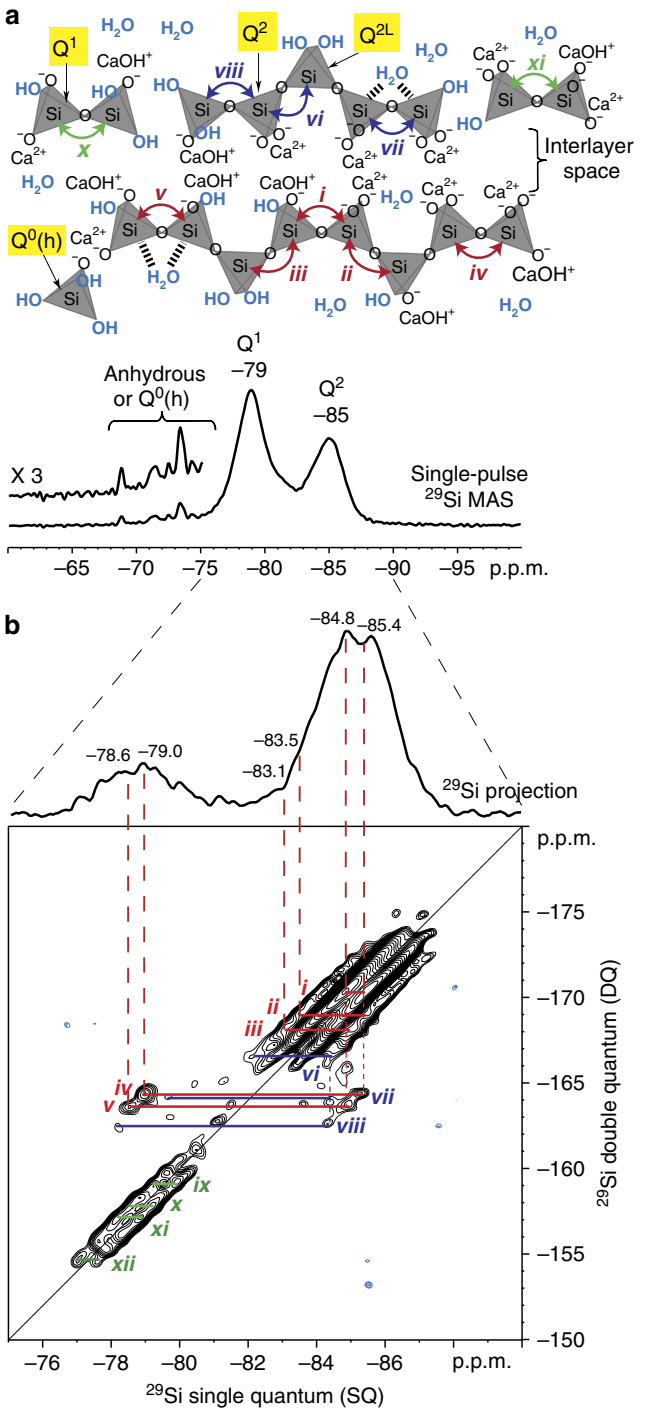

Figure 4 | Molecular structures and silicate site connectivities in partially polymerized calcium-silicate-hydrates. (**a**,**b**) Solid-state (**a**) 1D single-pulse ^{29}Si MAS and (**b**) 2D *J*-mediated ^{29}Si{^{29}Si} correlation NMR spectra of hydrated (1.5 month, 25 °C) ^{29}Si-enriched triclinic Ca_3SiO_5. The lowest contour lines in the 2D spectrum are 9% of the maximum signal intensity. The 'double-quantum' filter used to acquire the spectrum in **b** enables selective detection of pairs of signals (*i*, *j*) from distinct ^{29}Si nuclei that are covalently bonded. Consequently, the 2D spectrum exhibits intensity correlations between ^{29}Si signals at distinct frequencies (ω_i, ω_j) from ^{29}Si-O-^{29}Si spin pairs (*i*, *j*) in the horizontal SQ dimension (isotropic ^{29}Si chemical shifts) and at the sum of these frequencies ($\omega_i + \omega_j$) in the vertical DQ dimension. Therefore, correlated intensities at these specific positions in the 2D spectrum unambiguously establish the presence of covalently bonded ^{29}Si silicate species corresponding to the distinct isotropic ^{29}Si chemical shifts. The inset in **a** shows a schematic diagram of the different silicate moieties present in the calcium-silicate-hydrates with double-headed arrows indicating the *J*-interactions in ^{29}Si-O-^{29}Si species that are established by the intensity correlations in the 2D spectrum, specifically from dimeric (green), pentameric (blue) or octameric (red) units. For sake of clarity, the calcium layers are not represented.

Discussion

The carefully synthesized ^{29}Si-enriched sample enables, for the first time, 2D *J*-mediated (through ^{29}Si-O-^{29}Si bonds) ^{29}Si{^{29}Si} NMR measurements that provide detailed insights regarding the different silicate species, their respective site connectivities, and relative populations, especially for previously unidentified discrete silicate moieties in the C-S-H. Consequently, the lengths of C-S-H

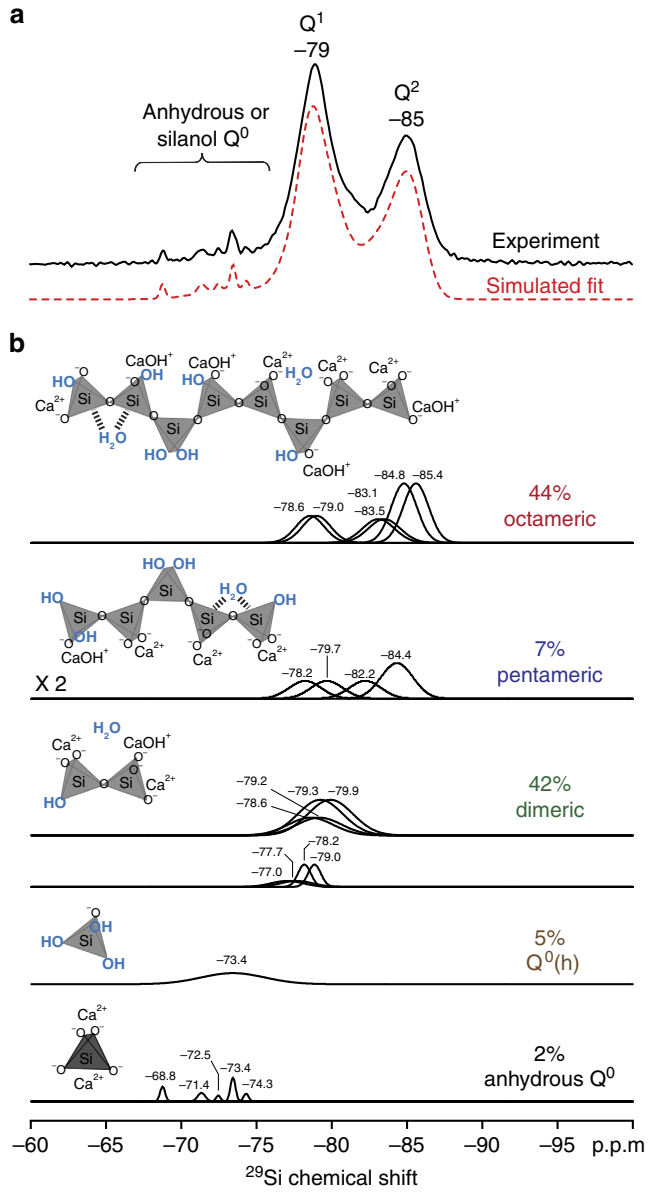

Figure 5 | Relative populations of ^{29}Si silicate species in hydrated triclinic Ca_3SiO_5. (**a**) Solid-state 1D single-pulse ^{29}Si MAS spectrum (black) of hydrated (1.5 month, 25 °C) ^{29}Si-enriched Ca_3SiO_5 and corresponding simulated fit (red) to the spectrum based on the signal decompositions shown in **b**. (**b**) Signal decompositions and relative populations of the different ^{29}Si moieties that comprise anhydrous Q^0, Q^0(h) and octameric, pentameric and dimeric C-S-H units, which contribute to the simulated fit (red) in **a**. Insets in **b** show schematic diagrams of the possible types of C-S-H units and the associated silicate moieties.

chains and the relative populations of associated silicate species are determined, which can be used to evaluate the validity of molecular models for Portland cement hydration that have been previously proposed in the literature[17,21,47]. This opens new perspective for understanding the complex molecular-level mechanical properties of C-S-H.

Solid-state ^{29}Si NMR measurements of ^{29}Si-enriched triclinic Ca_3SiO_5 also enable the transient silicate speciation and polymerization in the developing C-S-H structure to be monitored and quantified as a function of hydration time, especially during the crucial induction, acceleration and deceleration stages. Importantly, hydroxylated monomeric (Q^0(h)) silicate species can be detected and quantified by using ^{29}Si{^{1}H} CPMAS NMR measurements to monitor changes in surface composition with the progress of hydration. The NMR results presented here establish that non-hydrated Ca_3SiO_5 particle surfaces predominantly consist of hydroxylated Q^0 silicate species with negligible quantities of Q^1 and Q^2 hydration products, including for the pre-induction and induction stages of the hydration process. Such detailed insights of silicate-water mixtures have heretofore been challenging and often infeasible to determine by other characterization techniques due to the low absolute quantities, complicated structures and poor long-range order of the hydroxylated surface species. Compared with the induction period, the onset of silicate polymerization (that is, Q^1 and/or Q^2 species) during hydration corresponds to the formation of dimeric units in C-S-H during the acceleration stage, consistent with previous cement literature. Interestingly, during the deceleration stage the hydration rate reduces (at a hydration level of 50%) before any significant reduction of the Q^0(h) populations are observed at the Ca_3SiO_5 surface. This corresponds to a relatively fast decrease in the reaction rate compared with the rate of reduction of the hydroxylated species available for reaction at the surface, which indicates that part of the surface is likely covered by C-S-H products. These results are consistent with previous studies that suggest that the rate of hydration is controlled by the surface coverage of C-S-H species during the deceleration stage[37]. Calculations based on a shrinking core model (hydration reaction slows down due to consumption of the particles) indicate that for monodispersed spherical particles, a decrease in volume by a factor of 0.5 would be accompanied by a decrease in surface area by a factor 0.63 ($2^{-2/3}$). Ca_3SiO_5 particles are neither spherical nor monodisperse but the present NMR results are definitely not compatible with a shrinking core model. Consequently, the surface area available for reaction is clearly modified by the surface roughness produced by dissolution driven etching of the surface[38].

The relations directly observed here for the first time between surface passivation and etching phenomena on the one hand and the succession of the induction, acceleration and deceleration stages of hydration of Ca_3SiO_5 on the other hand, provide new understanding for the occurrence of this complex kinetic behaviour actually observed in a variety of silicate systems. Ca_3SiO_5, because of its high reactivity, constitutes an interesting model for understanding long term silicate hydration processes occurring during geochemical weathering or hydrothermal synthesis[23].

Methods

NMR spectroscopy. The ^{1}H and ^{29}Si NMR isotropic chemical shifts were referenced to tetramethylsilane using tetrakis(trimethylsilyl)silane [$((CH_3)_3Si_4)Si$] as a secondary standard[52]. All measurements were performed using zirconia MAS rotors and at room temperature. Solid-state 1D ^{29}Si NMR experiments were carried out using a Bruker Avance-III 500 spectrometer (magnetic field 11.7 T). Magic-angle-spinning (MAS) spectra were measured using a Bruker MAS NMR probe with 4 mm rotors, at spinning frequencies of 7 kHz, and without decoupling. The single-pulse ^{29}Si MAS NMR spectra were acquired with a $\pi/2$ pulse length of 6 µs, a recycle delay of 1,000 or 100 s, and 64 or 16 scans for the ^{29}Si-enriched non-hydrated and hydrated Ca_3SiO_5 samples, respectively. {^{1}H}^{29}Si CPMAS NMR spectra were recorded using a ^{1}H rf power of 93 kHz, a contact time of 5 ms, and recycle delay of 10 s. The number of scans was 184 for hydrated Ca_3SiO_5 samples and 2,000 for non-hydrated sample. Hartmann–Hahn matching was ensured by a ramp on the ^{29}Si rf field intensity. 2D {^{1}H}-^{29}Si heteronuclear dipolar correlation (HETCOR) experiments were conducted on a Bruker Avance-700 (16.4 T) spectrometer at ambient temperature, under 4 kHz MAS conditions, with a 7 ms CP contact time, recycle delay of 10 s and 66 t_1 increments of 50 µs each. Solid-state 2D J-mediated ^{29}Si{^{29}Si} DQ correlation NMR experiments were conducted using the refocused-INADEQUATE technique[39] and a 18.8 T Bruker AVANCE-III NMR spectrometer. The experiments were conducted under conditions of 12.5 kHz MAS using a Bruker 3.2 mm H-X double resonance probehead. The 2D ^{29}Si{^{29}Si} spectrum was acquired using a 2.5 µs ^{1}H $\pi/2$ pulse, 3.5 ms contact time for ^{29}Si{^{1}H} CP, 6.0 µs ^{29}Si $\pi/2$ pulses, SPINAL-64 ^{1}H decoupling[53], 152 t_1 increments, an incremental step size of 80 µs, a recycle delay of 2 s and 3,072 scans for each t_1 increment, which corresponds to an experimental time of 260 h (~11 days).

Hydration experiments. Paste for *in situ* NMR measurements was prepared by mixing 0.3 g of non-hydrated ^{29}Si-enriched Ca_3SiO_5 and 0.24 g of ultrapure water in a cylindrical 2 ml plastic vial for 3 min using a vortex mixer (Analog, VWR) at 2,500 r.p.m. With the help of a syringe and needle, part this paste was introduced as such in the zirconia MAS rotor thus enabling the acquisition of the NMR spectra during the reaction and avoiding any possible microstructural changes caused by the commonly used drying techniques[24]. After 6 h of hydration, the paste was removed from the ZrO_2 rotor to prevent its hardening inside the rotor, and the NMR measurements were continued on the part of the sample previously set aside and stored in the closed vial at room temperature. The kinetics of ^{29}Si-enriched Ca_3SiO_5 hydration were measured by isothermal calorimetry using a TAM Air microcalorimeter at 23 °C. One gram of ^{29}Si-enriched Ca_3SiO_5 was mixed with 0.8 g of ultrapure water under identical conditions as for samples prepared for NMR measurements. The paste was immediately sealed in a glass ampoule and placed in the isothermal calorimeter. The degree of reaction of ^{29}Si-enriched Ca_3SiO_5 was calculated by dividing the cumulative heat released at a certain time by the enthalpy of the hydration reaction of Ca_3SiO_5 ($-520\,J\,g^{-1}$ Ca_3SiO_5) (refs 54,55). Additional details of synthesis, Ca_3SiO_5 characterization and NMR quantitative analysis are reported in the Supplementary Methods and Supplementary Note 1.

References

1. Le Chatelier, H. *Recherches Expérimentales sur la Constitution des Mortiers Hydrauliques* (Doctoral thesis, Faculté des Sciences de Paris, 1887).
2. Nugent, M. A., Brantley, S. L., Pantano, C. G. & Maurice, P. A. The influence of natural mineral coatings on feldspar weathering. *Nature* **395,** 588–591 (1998).
3. Casey, W. H., Westrich, H. R., Banfield, J. F., Ferruzzi, G. & Arnord, W. G. Leaching and reconstruction at the surface of dissolving chain-silicate minerals. *Nature* **366,** 253–256 (1993).
4. Conradt, R. Chemical durability of oxide glasses in aqueous solutions. *J. Am. Ceram. Soc.* **91,** 728–735 (2008).
5. Cailleteau, C. *et al.* Insight into silicate-glass corrosion mechanisms. *Nat. Mater.* **7,** 978–983 (2008).
6. Cundy, C. S. & Cox, P. A. The hydrothermal synthesis of zeolites: history and development from the earliest days to the present time. *Chem. Rev.* **103,** 663–702 (2003).
7. Serrano, D. & Van Grieken, R. Heterogenous events in the crystallization of zeolites. *J. Mater. Chem.* **11,** 2391–2407 (2001).
8. Bullard, J. W. *et al.* Mechanisms of cement hydration. *Cement Concrete Res.* **41,** 1208–1223 (2011).
9. Taylor, H. F. W. *Cement Chemistry* (Thomas Telford, 1997).
10. Bullard, J. W. & Flatt, R. J. New insights into the effect of calcium hydroxide precipitation on the kinetics of tricalcium silicate hydration. *J. Am. Ceram. Soc.* **93,** 1894–1903 (2010).
11. Gartner, E. M. & Jennings, H. M. Thermodynamics of calcium silicate hydrates and their solutions. *J. Am. Ceram. Soc.* **70,** 743–749 (1987).
12. Juilland, P., Gallucci, E., Flatt, R. J. & Scrivener, K. S. Dissolution theory applied to the induction period in alite hydration. *Cement Concrete Res.* **40,** 831–844 (2010).
13. Nicoleau, L., Nonat, A. & Perrey, D. The di- and tricalcium silicate dissolutions. *Cement Concrete Res.* **47,** 14–30 (2013).
14. Nicoleau, L., Schreiner, E. & Nonat, A. Ion-specific effects influencing the dissolution of tricalcium silicate. *Cement Concrete Res.* **59,** 118–138 (2014).
15. Lasaga, A. C. & Luttge, A. Variation of crystal dissolution rate based on a dissolution stepwave model. *Science* **291,** 2400–2404 (2001).
16. Arvidson, R. S., Ertan, I. E., Amonette, J. E. & Luttge, A. Variation in calcite dissolution rates: A fundamental problem? *Geochim. Cosmochim. Acta* **67,** 1623–1634 (2003).
17. Richardson, I. G. Tobermorite/jennite- and tobermorite/calcium hydroxide-based models for the structure of C-S-H: applicability to hardened pastes of tricalcium silicate, β-dicalcium silicate, Portland cement, and blends of Portland cement with blast-furnace slag, metakaolin, or silica fume. *Cement Concrete Res.* **34,** 1733–1777 (2004).
18. Allen, A. J., Thomas, J. J. & Jennings, H. M. Composition and density of nanoscale calcium-silicate-hydrate in cement. *Nat. Mater.* **6,** 311–316 (2007).
19. Mishra, R. K., Flatt, R. J. & Heinz, H. Force field for tricalcium silicate and insight into nanoscale properties: cleavage, initial hydration, and adsorption of organic molecules. *J. Phys. Chem. C* **117,** 10417–10432 (2013).
20. Thomas, J. J. *et al.* Modeling and simulation of cement hydration kinetics and microstructure development. *Cement Concrete Res.* **41,** 1257–1278 (2011).
21. Qomi, M. J. A. *et al.* Combinatory molecular optimization of cement hydrates. *Nat. Commun.* **5,** 4960 (2014).
22. Brough, A. R., Dobson, C. M., Richardson, I. G. & Groves, G. W. *In situ* solid-state NMR studies of Ca_3SiO_5: hydration at room temperature and at elevated temperatures using ^{29}Si enrichment. *J. Mater. Sci.* **29,** 3926–3940 (1994).
23. Fischer, C., Arvidson, R. S. & Lüttge, A. How predictable are dissolution rates of crystalline material? *Geochim. Cosmochim. Acta* **98,** 177–185 (2012).
24. Zhang, J. & Scherer, G. W. Comparison of methods for arresting hydration of cement. *Cement Concrete Res.* **41,** 1024–1036 (2011).
25. Engelhardt, G. & Michel, D. *High-Resolution Solid-State NMR of Silicates and Zeolites* (John Wiley & Sons, 1987).
26. Bellmann, F., Damidot, D., Möser, B. & Skibsted, J. Improved evidence for the existence of an intermediate phase during hydration of tricalcium silicate. *Cement Concrete Res.* **40,** 875–884 (2010).
27. Rawal, A. *et al.* Molecular silicate and aluminate species in anhydrous and hydrated cements. *J. Am. Chem. Soc.* **132,** 7321–7337 (2010).
28. Cong, X. & Kirkpatrick, R. J. 17O MAS NMR investigation of the structure of calcium silicate hydrate gel. *J. Am. Ceram. Soc.* **79,** 1585–1592 (1996).
29. Durgun, E., Manzano, H., Kumar, P. V. & Grossman, J. C. The characterization, stability, and reactivity of synthetic calcium silicate surfaces from first principles. *J. Phys. Chem. C* **118,** 15214–15219 (2014).
30. Garrault, S., Behr, T. & Nonat, A. Formation of the C–S–H layer during early hydration of tricalcium silicate grains with different sizes. *J. Phys. Chem. B* **110,** 270–275 (2006).
31. Kumar, A., Bishnoi, S. & Scrivener, K. L. Modelling early age hydration kinetics of alite. *Cement Concrete Res.* **42,** 903–918 (2012).
32. Gonzalez-Teresa, R., Dolado, J. S., Ayuela, A. & Gimel, J. C. Nanoscale texture development of C-S-H gel: a computational model for nucleation and growth. *Appl. Phys. Lett.* **103,** 234105 (2013).
33. Ioannidou, K., Pellenq, R. J. M. & Del Gado, E. Controlling local packing and growth in calcium-silicate-hydrate gels. *Soft Matter* **10,** 1121–1133 (2014).
34. Bishnoi, S. & Scrivener, K. L. Studying nucleation and growth kinetics of alite hydration using μic. *Cement Concrete Res.* **39,** 849–860 (2009).
35. Tzschichholz, F. & Zanni, H. Global hydration kinetics of tricalcium silicate cement. *Phys. Rev. E* **64,** 016115 (2001).
36. Garrault, S., Finot, E., Lesniewska, E. & Nonat, A. Study of C-S-H growth on C3S surface during its early hydration. *Mater. Struct.* **38,** 435–442 (2005).
37. Bullard, J. W., Scherer, G. W. & Thomas, J. J. Time dependent driving forces and the kinetics of tricalcium silicate hydration. *Cement Concrete Res.* **74,** 26–34 (2015).
38. Nicoleau, L. & Bertolim, M. A. Analytical model for the alite (C3S) dissolution topography. *J. Am. Ceram. Soc.* http://dx.doi.org/10.1111/jace.13647 (2015).
39. Lesage, A., Bardet, M. & Emsley, L. Through-bond carbon-carbon connectivities in disordered solids by NMR. *J. Am. Chem. Soc.* **121,** 10987–10993 (1999).
40. Fyfe, C. A. & Brouwer, D. H. Optimization, standardization, and testing of a new NMR method for the determination of zeolite host-organic guest crystal structures. *J. Am. Chem. Soc.* **128,** 11860–11871 (2006).
41. Cadars, S., Brouwer, D. H. & Chmelka, B. F. Probing local structures of siliceous zeolite frameworks by solid-state NMR and first-principles calculations of ^{29}Si-O-^{29}Si scalar couplings. *Phys. Chem. Chem. Phys.* **11,** 1825–1837 (2009).
42. Köster, T. K.-J. *et al.* Resolving the different silicon clusters in $Li_{12}Si_7$ by ^{29}Si and ^{6,7}Li solid-state NMR spectroscopy. *Angew. Chem. Int. Ed. Engl.* **50,** 12591–12594 (2011).
43. Shayib, R. M. *et al.* Structure-directing roles and interactions of fluoride and organocations with siliceous zeolite frameworks. *J. Am. Chem. Soc.* **133,** 18728–18741 (2011).
44. Brunet, F., Bertani, P., Charpentier, T., Nonat, A. & Virlet, J. Application of 29Si homonuclear and 1H-29Si heteronuclear NMR correlation to structural studies of calcium silicate hydrates. *J. Phys. Chem. B* **108,** 15494–15502 (2004).
45. Cadars, S., Lesage, A. & Emsley, L. Chemical shift correlations in disordered solids. *J. Am. Chem. Soc.* **127,** 4466–4476 (2005).
46. Rejmak, P., Dolado, J. S., Stott, M. J. & Ayuela, A. ^{29}Si NMR in cement: a theoretical study on calcium silicate hydrates. *J. Phys. Chem. C* **116,** 9755–9761 (2012).
47. Pellenq, R. *et al.* A realistic molecular model of cement hydrates. *Proc. Natl Acad. Sci. USA* **106,** 16102–16107 (2009).
48. Ayuela, A. *et al.* Silicate chain formation in the nanostructure of cement-based materials. *J. Chem. Phys.* **127,** 164710 (2007).
49. Chen, J. J. *et al.* Solubility and structure of calcium silicate hydrate. *Cement Concrete Res.* **34,** 1499–1519 (2004).
50. Kulik, D. A. Improving the structural consistency of C-S-H solid solution thermodynamic models. *Cement Concrete Res.* **41,** 477–495 (2011).
51. Richardson, I. G. Model structures for C-(A)-S-H (I). *Acta Crystallogr. B* **70,** 903–923 (2014).
52. Hayashi, S. & Hayamizu, K. Chemical shift standards in high-resolution solid-state NMR (1) 13C, 29Si, and 1H nuclei. *Bull. Chem. Soc. Jpn* **64,** 685–687 (1991).
53. Fung, B. M., Khitrin, A. K. & Ermolaev, K. An improved broadband decoupling sequence for liquid crystals and solids. *J. Magn. Reson.* **142,** 97–101 (2000).

54. Thomas, J. J., Jennings, H. M. & Chen, J. J. Influence of nucleation seeding on the hydration mechanisms of tricalcium silicate and cement. *J. Phys. Chem. C* **113,** 4327–4334 (2009).
55. Damidot, D. & Nonat, A. C3S hydration in diluted and stirred suspensions: (I) study of two kinetic steps. *Adv. Cem. Res.* **6,** 27–35 (1994).

Acknowledgements

This research was supported by the Commission for Technology and Innovation (CTI project number 15846.1), the US Federal Highway Administration (FHWA) under agreement No. DTFH61-12-H-00003 and by Halliburton, Inc. (Any opinions, findings and conclusions or recommendations expressed in this publication are ours and do not necessarily reflect the view of the US Federal Highway Administration). Funding was also provided by the program 'Germaine de Staël' and a mobility fellowship from the French Embassy in Bern. We thank Dr R. Verel (ETH Zürich), Dr M Plötze (ETH Zûrich) and S. Mantellato (ETH Zürich) for their assistance in the 1D ^{29}Si NMR, XRD and BET surface area measurements, respectively. D. Marchon (ETH Zürich) is also thanked for her support in the development of the synthesis protocol of Ca_3SiO_5. The solid-state 2D *J*-mediated ^{29}Si{^{29}Si} correlation NMR measurements were conducted using the UCSB Materials Research Laboratory (MRL) Shared Experimental Facilities that are supported by the MRSEC Program of the US National Science Foundation under Award No. DMR 1121053; a member of the NSF-funded Materials Research Facilities Network (www.mrfn.org).

Authors contributions

E.P. was the main investigator. She developed the synthesis of the Ca_3SiO_5 samples, designed and carried out the characterization and calorimetry studies. J.-B.d.E.d.L., R.J.F. and M.P. designed the project. B.F.C. proposed the 2D J-mediated and relaxation NMR experiments. E.P., A.S.A., J.-B.d.E.d.L. and R.P.S. performed the NMR experiments. All authors contributed to the analyses of the results and the writing of the manuscript.

Additional information

Supplementary Information accompanies this paper at http://www.nature.com/naturecommunications

Competing financial interests: The authors declare no competing financial interests.

Reprints and permission information is available online at http://npg.nature.com/reprintsandpermissions/

How to cite this article: Pustovgar, E. *et al.* Understanding silicate hydration from quantitative analyses of hydrating tricalcium silicates. *Nat. Commun.* 7:10952 doi: 10.1038/ncomms10952 (2016).

Supplementary Information

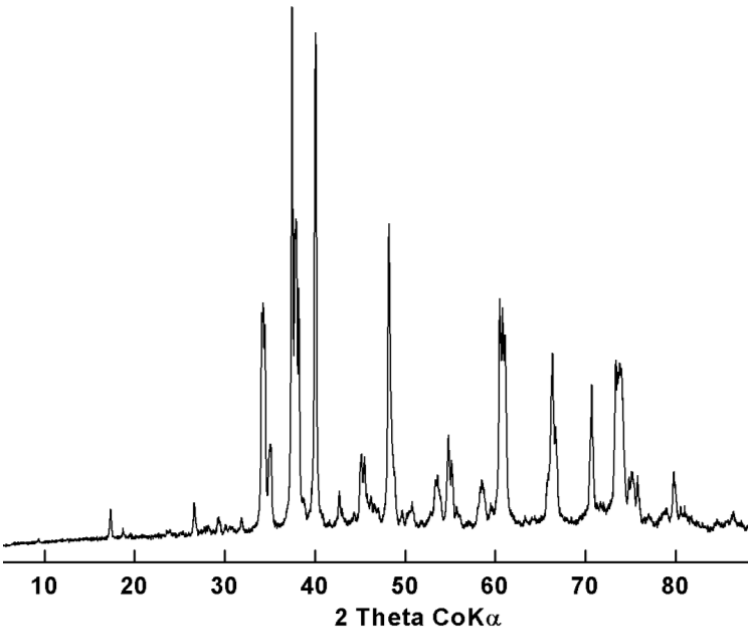

Supplementary Figure 1. XRD pattern of as-synthesized pure triclinic ^{29}Si-enriched Ca_3SiO_5.

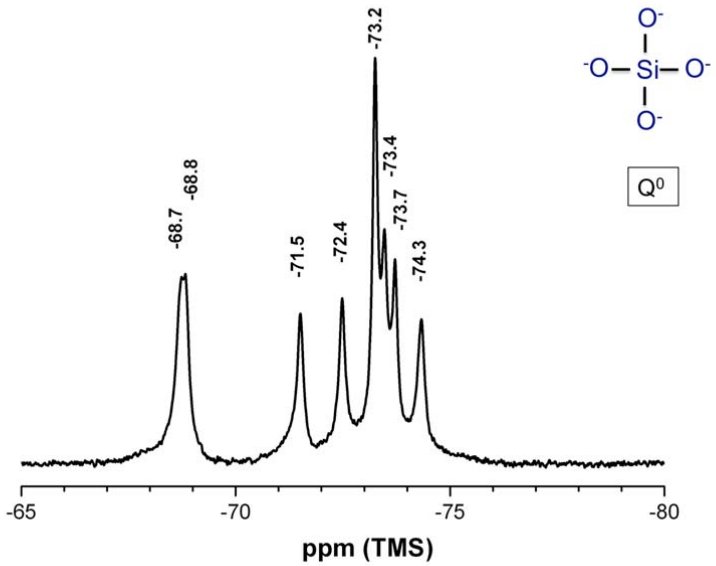

Supplementary Figure 2. Solid-state ^{29}Si MAS NMR spectrum of as-synthesized ^{29}Si-enriched Ca_3SiO_5.

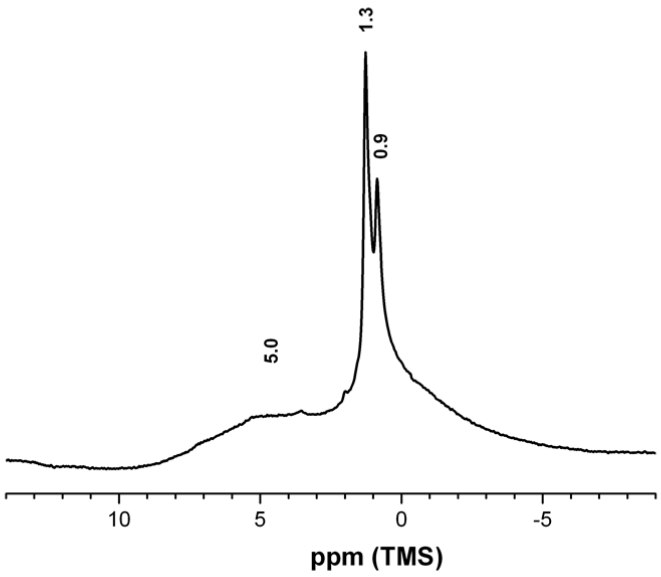

Supplementary Figure 3. Solid-state ^{1}H MAS NMR spectrum of as-synthesized (before hydration experiments) ^{29}Si-enriched Ca_3SiO_5.

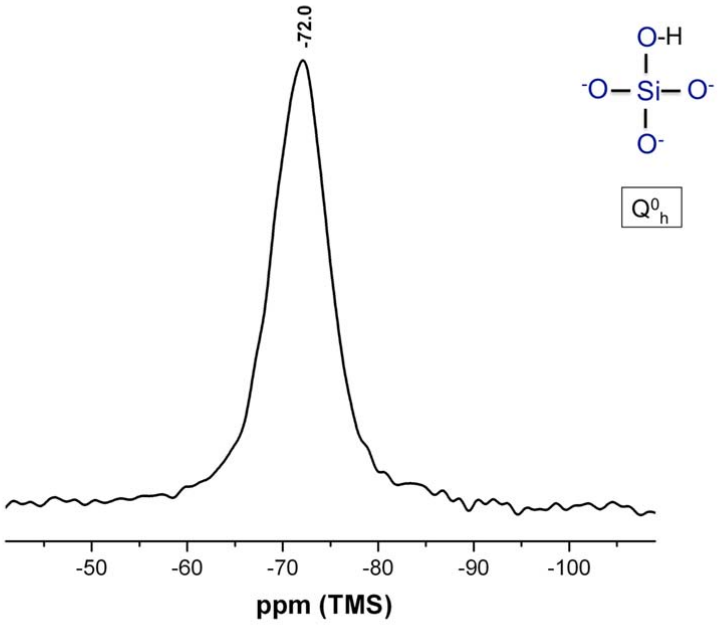

Supplementary Figure 4. Solid-state ^{1}H – ^{29}Si CPMAS NMR spectrum of as-synthesized (before hydration experiment) ^{29}Si-enriched Ca_3SiO_5.

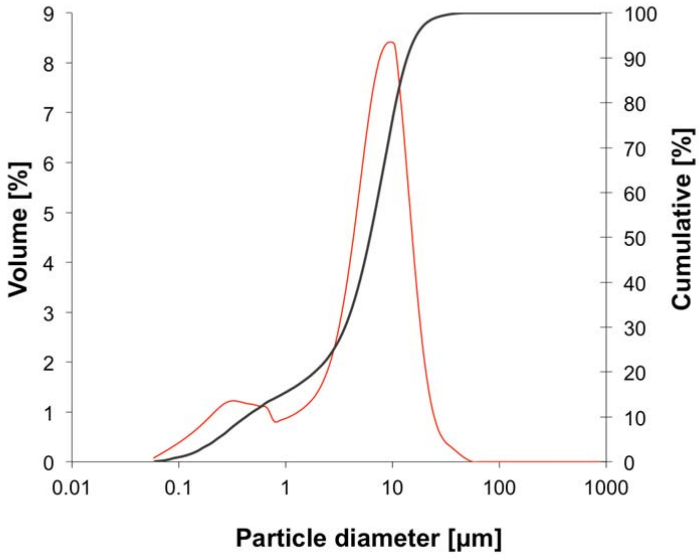

Supplementary Figure 5. Particle size distribution of as-synthesized ^{29}Si-enriched Ca_3SiO_5.

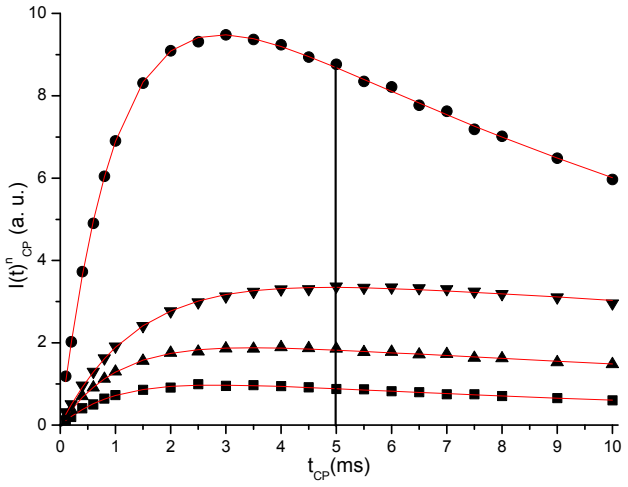

Supplementary Figure 6. Polarization growth curve on Ca_3SiO_5 hydrated for 90 days. The bar marks the 5 ms contact time used to measure $I^n_{cp}(t)$ and from which the quantitative intensities $I^n_{cp}(t)'$ are derived. The continuous curves are fits to Supplementary Equation (7).

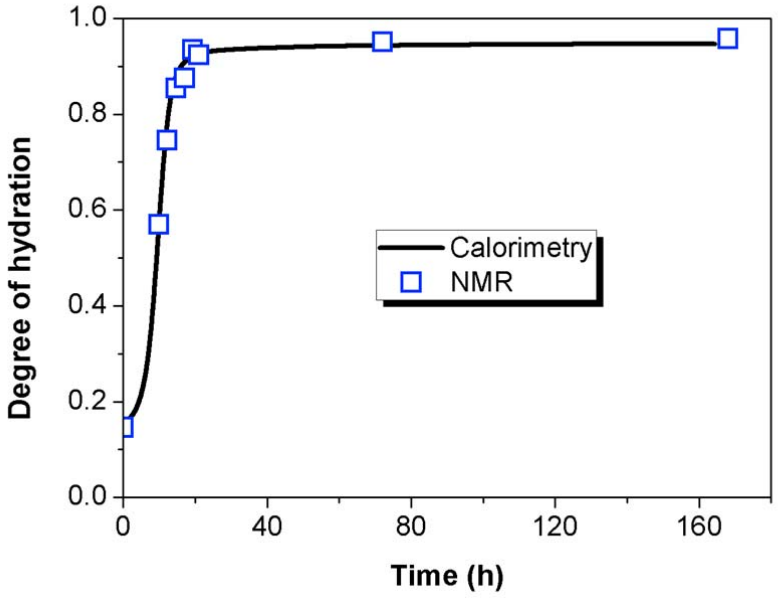

Supplementary Figure 7. Comparison of the degree of reaction calculated from quantitative NMR results (in red) and isothermal calorimetry (in blue).

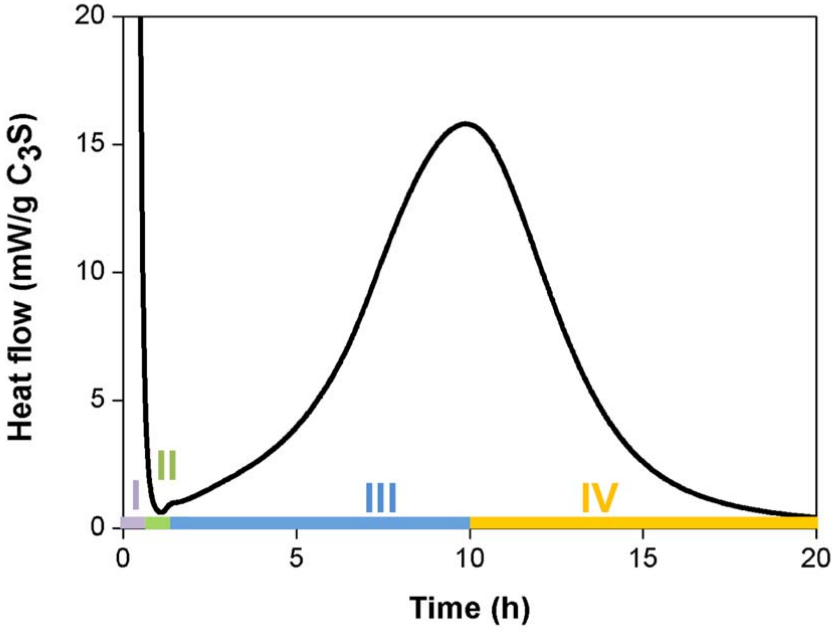

Supplementary Figure 8. Isothermal calorimetry curve of Ca_3SiO_5 hydration. Four regions are typically identified based on the heat flow profile with increasing hydration time, including pre-induction (I), induction (II), acceleration (III), and deceleration (IV) stages.

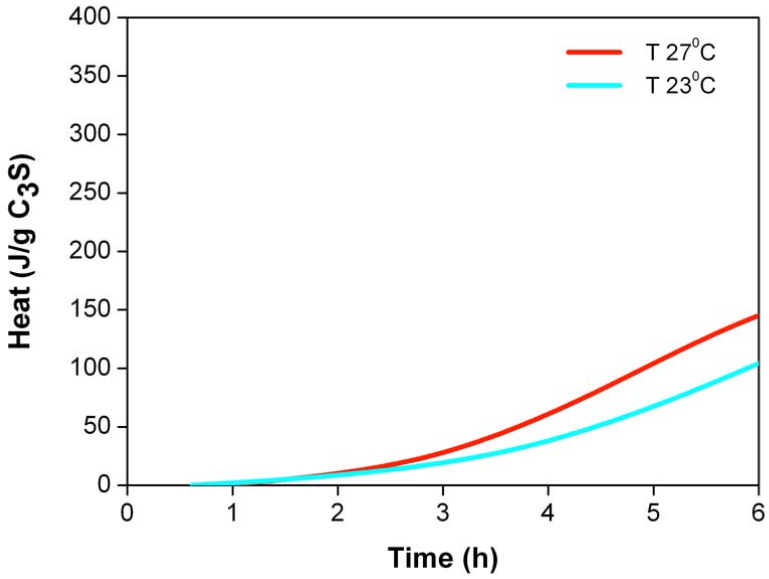

Supplementary Figure 9. Hydration of Ca_3SiO_5 at 23 and 27 ^{0}C studied by isothermal calorimetry.

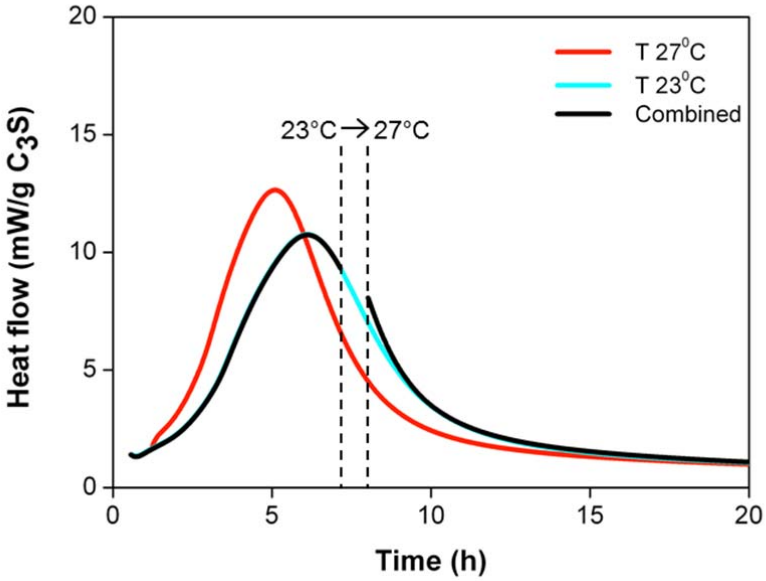

Supplementary Figure 10. Heat release rate during hydration of Ca_3SiO_5 studied by isothermal calorimetry at 23 ^{0}C (cyan), 27 ^{0}C (red) and under a combined cycle of 7 h at 23 ^{0}C followed by an increase to 27 ^{0}C (black). The gap corresponds the time needed to switch the sample between the calorimeters and to stabilize the equipment.

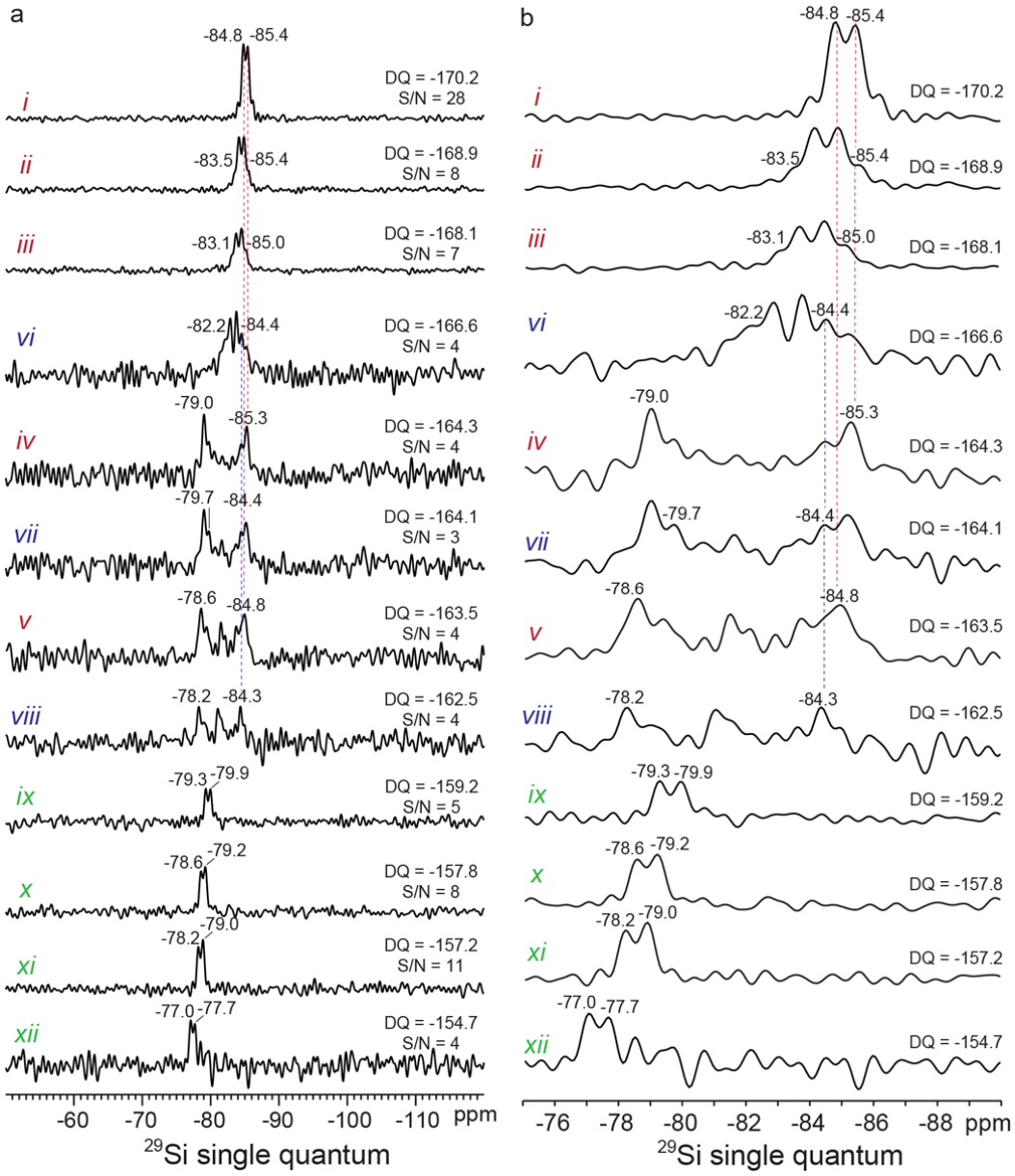

Supplementary Figure 11. Site connectivity in C-S-H. a,b, 1D ^{29}Si spectra that are slices at different double-quantum (DQ) ^{29}Si chemical shifts from the 2D *J*-mediated ^{29}Si{^{29}Si} correlation NMR spectrum (Supplementary Figure 4b). Different pairs of intensity correlations (labelled by roman numerals in the 2D spectrum) between ^{29}Si signals at distinct frequencies (ω_i, ω_j) in the single-quantum (SQ) dimension (isotropic ^{29}Si chemical shifts) and at the sum of these frequencies ($\omega_i + \omega_j$) in the DQ dimension (indicated for each slice) unambiguously establish that the associated distinct ^{29}Si species (i, j) are covalently bonded

through a shared bridging oxygen atom. The spectra in (**b**) are identical to those in (**a**), but shown over a narrower single-quantum ^{29}Si chemical shift range (-75 to -90 ppm). The DQ ^{29}Si chemical shifts and signal-to-noise ratios (S/N) are indicated for each slice.

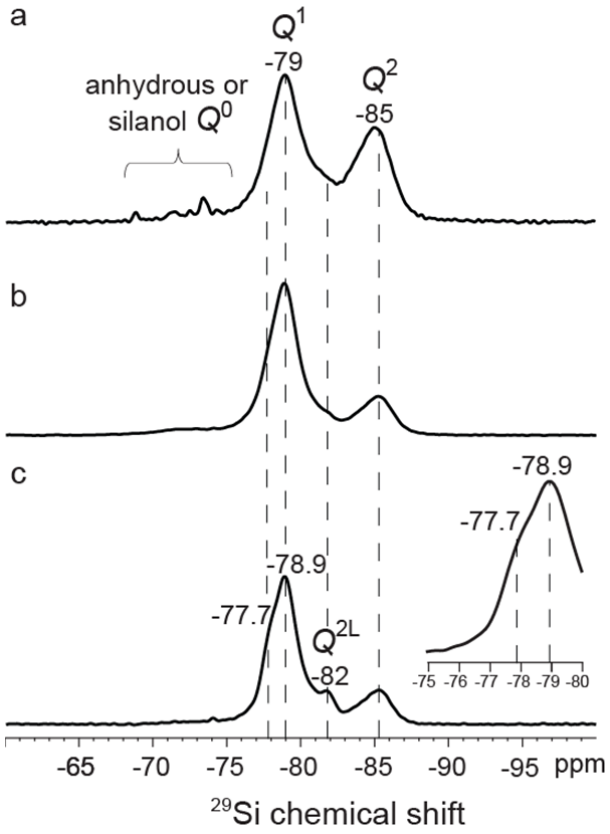

Supplementary Figure 12. Different extents of silicate polymerization in C-S-H. **a-c**, Solid-state 1D (**a**) single-pulse ^{29}Si, (**b**) ^{29}Si{^{1}H} cross-polarization (CP), and (**c**) T_2-filtered ^{29}Si{^{1}H} CP MAS spectra of hydrated (1.5 month, 25 °C) ^{29}Si-enriched triclinic Ca_3SiO_5. The spectra were acquired at (**a**) 18.8 T, 12.5 kHz MAS, 25 °C or (**b, c**) 11.7 T, 4.6 kHz MAS, 25 ºC. In (**c**), a nuclear spin-spin (T_2) relaxation-time filter (t_{T2}) of 20 ms and a ^{29}Si 180° pulse were applied before signal detection, to detect selectively ^{29}Si species with long (>20 ms) T_2 relaxation times. The inset in (**c**) shows a magnified version of the spectrum over the chemical shift range of -75 to -80 ppm.

Supplementary Table 1. Fit parameters for each type of ^{29}Si environments in hydrated Ca_3SiO_5.

One-pulse spectra										
chemical environment	Q^0							Q^1	Q^{2L}	Q^2
chemical shift (ppm)	-68.82	-71.55	-72.53	-73.29	-73.52	-73.77	-74.36	-78.7	-81.5	-85.2
width (ppm)	0.3	0.23	0.2	0.17	0.18	0.17	0.18	2.1	2.74	2.37
xG/(1-x)L	0	0	0	0	0	0	0	0.1	0.79	1
^{1}H - ^{29}Si cross polarization spectra										
chemical environment	Q^0(h)							Q^1	Q^{2L}	Q^2
chemical shift (ppm)	-72.1							-78.7	-81.5	-85.2
width (ppm)	6.84							2.44	1.3	2.73
xG/(1-x)L	0.68							0.1	0.79	1

SupplementaryTable 2. Average measured $\bar{k}^n$ values.

$\bar{k}^1$	$\bar{k}^2$
1.06 ± 0.02	0.94 ± 0.25

Supplementary Methods

Synthesis of ^{29}Si-enriched Ca_3SiO_5

Pure tricalcium silicate (Ca_3SiO_5) with ^{29}Si isotopic enrichment was synthesized by the solid state reaction method:

$$3\ CaCO_3 + SiO_2 \longrightarrow Ca_3SiO_5 + CO_2\uparrow \quad (1)$$

Precursors $CaCO_3$ (≥99 %, Sigma Aldrich) and SiO_2 (99.9 % enriched in ^{29}Si, Cortecnet) in 2.94 : 1 mass ratio were dry homogenized in a turbula for 24 h. Batches of approximately half a gram of the resulting powder were pressed into 1 cm pellets under a 25 kN load and fired afterwards in a platinum crucible at 1600 °C for 8 h. Since the triclinic Ca_3SiO_5 is a metastable phase, which tends to dissociate into CaO and Ca_2SiO_4,[1] pellets were quenched by fast cooling under an air gun. To reach the full transformation of the starting materials into the desired triclinic phase, the whole procedure was repeated 4 times, until no reflections due to free lime (CaO) were observed by X-ray diffraction.

Loss of SiO_2 during the homogenization process was unavoidable due to the strong electrostatic attraction of SiO_2 particles to the walls of the plastic container. Consequently, deviation from the stoichiometric ratio was necessary to prevent CaO from remaining in the final material.

The final material was ground using an agate mortar and then with absolute ethanol in a micronizing mill (McCrone) with agate grinding elements for 10 min. Absolute ethanol was used to ensure a better dispersion of the particles and to prevent heating that may otherwise result in undesirable structural modifications of the Ca_3SiO_5.

Characterization

^{29}Si-enriched Ca_3SiO_5 was characterized by X-ray diffraction (Supplementary Figure 1) using a Bruker AXS D8 diffractometer (Co K_α, λ = 1.7903 Å). 2θ was scanned between 4 and 90º by steps of 0.02º. The X-ray tube was operated at 40 kV and 30 mA. Rietveld

analyses were performed using the AutoQuan software and confirmed the triclinic crystal structure of the final material establishing the absence of any significant amounts of impurities with long-range structural order (refinement factor "weighted pattern" R_{wp} = 8.7 %).

The ^{29}Si-enriched Ca_3SiO_5 was also characterized by solid-state nuclear magnetic resonance (NMR) using ^{29}Si, ^{1}H one-pulse and ^{1}H-^{29}Si cross-polarization (CP) experiments. The ^{29}Si one-pulse NMR spectrum (Figure S2) shows 8 ^{29}Si resonances corresponding to the 9 distinct crystallographically inequivalent Si-sites in triclinic Ca_3SiO_5 (two overlapping ^{29}Si resonances are observed at -73.2 ppm).[2] With the help of ^{1}H one-pulse and ^{1}H-^{29}Si CP MAS NMR, it was possible to retrieve information concerning the initial state of the sample. It was found out that the material adsorbed water either during storage or milling since peaks at 0.9 ppm (-Ca-O-H), 1.3 ppm (-Si-O-H) and 5.0 ppm (H_2O) were observed in the ^{1}H NMR spectrum (Supplementary Figure 3). The ^{1}H – ^{29}Si CP NMR spectrum exhibited a signal centered at -72 ppm, which confirmed the presence of Q^0(h) (hydroxylated) species, even before mixing with water (Supplementary Figure 4).

The specific particle size distribution (Supplementary Figure 5) was measured by laser diffraction (Mastersizer, Malvern Instruments) after dispersion of the ^{29}Si-enriched Ca_3SiO_5 in isopropanol.

The surface area of the final Ca_3SiO_5 powder was 4.38 ± 0.02 m^2 / g. It was measured using a BET multi-point physisorption apparatus (Micromeritics Tristar II 3020). The sample was degassed in an external degassing station (VacPrep 061 from Micromeritics) at 200 °C for 1 h.

Supplementary Note 1. Quantitative comparison between isothermal calorimetry and NMR

Quantitative analysis of the NMR spectra.

The originality of the NMR results presented here lies mainly in their quantitative analysis. This is not trivial as cross-polarisation experiments are known to provide signal intensities that depend on several parameters, namely the Hartman-Hahn matching, the relaxation rates, the dipolar coupling, molecular mobility, and the extent of the proton bath. It is thus important to provide in detail the procedure followed that allowed seamless quantification based on the cross-polarisation and one-pulse experiments.

All one-pulse NMR experiments were performed with identical acquisition conditions. The same is true for the cross polarisation experiments (see Methods).

From the NMR spectra in the frequency domain, the integrated intensity corresponding to each chemical environment Q^n, was determined by decomposition of the ^{29}Si one-pulse and ^{1}H-^{29}Si CP MAS spectra using the program DMFit 2011.[3] To fit the signals a mixture of Gaussian (G) and Lorentzian (L) functions was applied as a model, which was kept constant together with the position and width for each specific resonance throughout the analyses of the NMR spectra (Supplementary Table 1).

After all integrated intensities were obtained, they were normalized to the number of scans, receiver gain and mass of Ca_3SiO_5 used for the measurements. The normalized intensities obtained by one-pulse and cross-polarization at a given time t are noted $I^n_{op}(t)$ and $I^n_{cp}(t)$ respectively.

Because a fully relaxed one-pulse NMR signal is directly proportional to the number of exited spins (here ^{29}Si) and because the number of ^{29}Si atoms introduced in the rotor is constant for a given hydration experiment, $I^n_{op}(t)$ can be expressed directly in arbitrary units of atoms of Si per mass of Ca_3SiO_5.

In contrast, the cross-polarization NMR spectra are affected by the spins relaxation and polarization transfer dynamics.[4] In samples with natural abundance ^{29}Si, the heat capacity of the silicon spin systems can be neglected compared to the one of the protons. Considering further that the relaxation of the silicon nuclei is much slower than the one of the protons, the cross-polarization dynamics between the ^{29}Si and the ^{1}H can be modelled as the superimposition of two first-order kinetics, namely the one of the ^{1}H relaxation in the rotating frame and the one of the polarization transfers between each ^{29}Si species and a unique ^{1}H bath.[5] In ^{29}Si enriched samples however, the assumption that the ^{29}Si spin heat capacities can be neglected versus the one of the ^{1}H falls. Consequently, there is no analytical solution to the set of differential equations describing the polarization intensity as a function of the contact time and the only option is to assess the relative heat capacities of each silicon spin bath by numerical modelling, as discussed by I. Klur in his doctoral thesis.[6] To avoid this lengthy procedure, it was preferable to calibrate the cross polarization response at a given contact time with respect to the quantitative one-pulse response. The following procedure was followed.

At a given contact time (5 ms), $I_{cp}^{n}(t)$ is measured (note that t is the hydration time, not the contact time of the cross polarization experiment) (Supplementary Figure 6). $I_{cp}^{n}(t)$ is proportional to the number of ^{29}Si spins but the proportionality constant (k^n) between the quantitative one pulse and the cross polarization intensities for the chemical environment Q^n,

$$k^n = \frac{I_{op}^{n}(t)}{I_{cp}^{n}(t)}, \qquad (2)$$

is an unknown function of the experimental conditions (Hartman-Hahn mismatch, rotation speed, contact time). It strongly depends on the acquisition conditions of the cross polarization spectra but will be a constant for a given chemical environment if these conditions are not varied as is the case in the present study. k^n is thus obtained by

comparison of the cross polarization intensities, $I_{cp}^{n}(t)$, with the quantitative one pulse ones, $I_{op}^{n}(t)$, at hydration times when both experiments provide a satisfactory signal to noise ratio. In practice, $k^{n}(t)$ is evaluated for hydration time *t* 21 h, 72 h, 168 h and 672 h, and the average $\overline{k}^{n}$ is calculated. The values are reported in the Supplementary Table 2.

At shorter time when only the cross polarization spectra can be obtained, this allowed to estimate a quantitative cross-polarization "one pulse-like" intensity, $I_{cp}^{n}(t)'$, by inverting Supplementary Equation (2)

$$I_{cp}^{n}(t)' = \overline{k}^{n} \times I_{cp}^{n}(t) \tag{3}$$

Since the $Q^0(h)$ species is a minor occurrence not revealed with sufficient resolution by one-pulse NMR, $\overline{k}^{0(h)}$ is not measurable in that manner. It was thus assumed that the true proportion of the $Q^0(h)$ resonance in the cross-polarization spectra was close to the one in the one-pulse spectra (which is equivalent to make the approximation of a common $\overline{k}^{n}$ value for all silicon species)

$$\frac{I_{cp}^{0(h)}(t)'}{I_{cp}^{1}(t)' + I_{cp}^{2}(t)'} = \frac{I_{cp}^{0(h)}(t)}{I_{cp}^{1}(t) + I_{cp}^{2}(t)} \tag{4}$$

and thus that $I_{cp}^{0(h)}(t)'$ can be estimated from the one-pulse and cross-polarization spectra decomposition through

$$I_{cp}^{0(h)}(t)' = \left[\overline{k}^{1} I_{cp}^{1}(t) + \overline{k}^{2} I_{cp}^{2}(t)\right] \frac{I_{cp}^{0(h)}(t)}{I_{cp}^{1}(t) + I_{cp}^{2}(t)} \tag{5}$$

When the Q^1 and Q^2 resonances where not observable in the cross polarization spectra (t < 1h), $I_{cp}^{0}(t < 1h)'$ was obtained simply by comparing with the intensity at later time:

$$I_{cp}^{0(h)}(t \le 1h)' = I_{cp}^{0(h)}(t > 1h)' \frac{I_{cp}^{0(h)}(t \le 1h)}{I_{cp}^{0(h)}(t > 1h)} \tag{6}$$

This simplified procedure is an approximation as in principle, the polarisation transfer efficiency, and thus the conversion coefficient k is expected to differ for each Q^n resonance. This approximation was validated in the following manner. On a selected sample (hydration time 90 days), the quantitative intensity was extracted from a full polarisation signal build-up curve (Supplementary Figure 6), neglecting the heat capacity of the silicon spin bath using the usual polarization growth relation and adjusting the polarization transfer and relaxation parameters T_{CP} and $T_{1\rho}{}^{H}$

$$I_{cp}^{n}(t) = I_{cp}^{n}(t)'\alpha\frac{1}{1-T_{cp}/T_{1\rho}^{H}}\left[\exp\left(-t_{cp}/T_{1\rho}^{H}\right)-\exp\left(-t_{cp}/T_{cp}\right)\right] \quad (7)$$

where the Hartman-Hahn mismatch α only acts as a constant scaling factor.

The resulting relative intensities were found to be within 5% of the ones obtained by our simplified procedure.

Finally, $Q^n(t)$, the proportion of silicon atoms in each Q^n environment in arbitrary units at hydration time t is obtained from the cross polarization spectra through

$$Q^{n}\left(t\right) = I_{cp}^{n}(t)' = \overline{k}^{n} \times I_{cp}^{n}(t) \quad (8)$$

for hydration times up to 10 h,

and from the one-pulse spectra directly through

$$Q^{n}\left(t\right) = I_{op}^{n}(t) \quad (9)$$

for longer hydration times.

Validation of the NMR quantitative analysis by comparison with isothermal calorimetry.

The degree of reaction (α) was calculated based on NMR quantitative analyses and compared with the value obtained by calorimetric measurement (Supplementary Figure 7). The values based on NMR data were calculated according to the following equations:

$$\alpha = 1-\frac{Q^{0}\left(t\right)}{Q^{0}\left(t=0\right)} \quad (10)$$

and

$$\alpha = \frac{Q^{0(h)}(t) + Q^{1}(t) + Q^{2}(t)}{Q^{0}(t=0)} \tag{11}$$

The NMR data matched the calorimetry results thus establishing the validity of the NMR quantitative analysis.

Supplementary Note 2. Isothermal calorimetry

The reaction of Ca_3SiO_5 with water is exothermic and, according to isothermal calorimetry, four main stages can be distinguished in the reaction of Ca_3SiO_5 with water (Supplementary Figure 8). The first one, the pre-induction period, is normally attributed to a rapid hydrolysis of the Ca_3SiO_5 surface releasing Ca^{2+}, OH^- and $H_2SiO_4^{2-}$ ions into solution. This is followed by a step with low reaction rate called the induction period (II), the origin of which has so far been poorly understood. Large amounts of C-S-H and $Ca(OH)_2$ are precipitated during the subsequent acceleration period (III), where nucleation and growth of the hydration products is the rate-controlling step. Finally, during the deceleration period (IV), C-S-H densification results in a decrease in the rate of silicate dissolution.

Since the sample temperature in the in-situ NMR measurements may deviate from ”room temperature” as a result of frictional heating during MAS experiments, calorimetric measurements were performed to assess potential frictional heating artefacts (Supplementary Figure 9). Indeed, this effect has been evaluated to account for a 4 K increase under our experimental conditions using the lead nitrate procedure.[7,8] Following our protocol for the NMR measurements, after 6 h of hydration the paste was removed from the ZrO_2 rotor to prevent its hardening inside the rotor and the subsequent loss of the rotor. The NMR measurements were continued on the part of the sample previously set aside in the closed vial and stored at room temperature.

The maximum possible consequences of a 4 K temperature variation are illustrated with the isothermal calorimetry measurements represented in Supplementary Figures 9 and 10. These were run with Ca_3SiO_5 paste at 27 and 23°C. The first three hours are identical, with a difference emerging only between 3 and 6 hours. In fact, this explains the slight observed difference at that time in the comparison between NMR and calorimetry data of Figure 2c. The cumulative effect of this temperature variation was appreciated by measuring the heat

release of the paste at 23°C for the first 7 h and then moving the sample to another calorimeter set at 27°C for the remaining experimental time. The heat flow (and thus the advancement of hydration) obtained during this measurement is very close to the one observed at 23°C. It can thus be concluded that the effect of the frictional heating during MAS is negligible under our experimental conditions.

Supplementary Note 3. Final C-S-H structure

The quantitative single-pulse ^{29}Si MAS spectrum (Supplementary Figure 12a) reveals signals from all anhydrous and hydrated ^{29}Si species, including Q^0, Q^1, and Q^2 moieties, as previously discussed in the main text of the manuscript. In contrast, the ^{29}Si{^{1}H} CPMAS experiment selectively detects ^{29}Si nuclei that are dipole-dipole-coupled to ^{1}H nuclei and thus are in close (<1 nm) molecular-level proximity. Correspondingly, the ^{29}Si{^{1}H} CPMAS spectrum exhibits ^{29}Si signals centred at -73 ppm (from Q^0(h) species), -79 ppm (from hydrated Q^1 species), and -85 ppm (from hydrated Q^2 species) that arise from ^{29}Si species in silicate hydration products. The relative intensities of the ^{29}Si signals in the ^{29}Si{^{1}H} CPMAS spectrum depend on the strengths of the heteronuclear ^{29}Si-^{1}H dipole-dipole couplings, which are determined by the molecular proximities and mobility of the associated chemical species. Nevertheless, signals with similar isotropic ^{29}Si chemical shifts, but with different relative intensities, are observed in the spectra in Supplementary Figure 12a,b.

By comparison, improved spectral resolution can be achieved by exploiting differences in the nuclear spin-spin (T_2) relaxation times of different hydrated silicate species to resolve their otherwise overlapping ^{29}Si signals. The T_2 relaxation times are sensitive to molecular structures and proximities of ^{29}Si species to dipole-dipole-coupled species, including ^{1}H moieties, and consequently can be used to distinguish their associated ^{29}Si NMR signals. This is accomplished by applying a T_2-filter (t_{T2}), during which signals from fast-relaxing ^{29}Si species ($T_2 < t_{T2}$) decay away, followed by a ^{29}Si 180° pulse (Hahn-echo-like technique) prior to the ^{29}Si NMR signal detection. The resulting signal consists of contributions exclusively from slow relaxing ($T_2 > t_{T2}$) ^{29}Si species in the calcium-silicate-hydrates. The calcium-silicate-hydrates exhibit strong through-space dipole-dipole-couplings between ^{29}Si and ^{1}H nuclei due to the abundance of ^{1}H species, including from hydroxyl moieties and water molecules, which are present in close (<1 nm) molecular proximity of the silicate

species. The magnitude of the T_2 relaxation time is attenuated by the increased strengths of the dipolar couplings, which consequently depend on molecular proximities and mobility. In ^{29}Si-enriched solids, as in the present case, the ^{29}Si-^{1}H dipole-dipole-couplings are further strengthened due to the significantly greater fractions of ^{29}Si nuclei compared to natural abundance conditions (4.7%), which correspondingly reduce the ^{29}Si T_2 relaxation times. These molecular-level structural differences are manifest in Supplementary Figure 12c as resolved ^{29}Si signals from the distinct silicate species, which were previously indistinguishable (Supplementary Figure 12a,b). For example, the T_2-filtered ^{29}Si{^{1}H} CPMAS spectrum exhibits partially resolved ^{29}Si signals at -77.7 and -78.9 ppm from chemically distinct Q^1 species that are associated with long T_2 relaxation times (>20 ms). Such structural differences in the ^{29}Si environments of Q^1 species that result in long T_2 relaxation times arise from their different proximities to water molecules and hydroxyl moieties, which influence the strengths of the heteronuclear ^{29}Si-^{1}H dipolar couplings. The ^{29}Si signal at -77.7 ppm (from Q^1 species) is consistent with the presence of dimeric C-S-H units that exhibit similar isotropic chemical shifts, as established based on the 2D *J*-mediated ^{29}Si{^{29}Si} spectrum (Fig. 5b). Additional ^{29}Si signal intensity is resolved at ca. 82 ppm and is attributed to Q^{2L} species. These results corroborate and complement the analyses of the 2D ^{29}Si{^{29}Si} spectrum, thereby increasing the confidence associated with the signal assignments and analysis of the silicate site connectivity.

Supplementary Note 4. Additional commentary on 2D *J*-mediated $^{29}Si\{^{29}Si\}$ NMR spectrum in Fig. 4b

Analyses of the pair correlated intensities in 2D $^{29}Si\{^{29}Si\}$ NMR spectrum of hydrated (1.5 month, 25 ºC) ^{29}Si-enriched Ca_3SiO_5 shown in Fig. 4b indicates the presence of pentameric C-S-H units, in addition to the octameric and dimeric units discussed in the main text of the manuscript.

A pentameric C-S-H unit consists of covalently bonded species with the sequence Q^1-Q^2-Q^{2L}-Q^2-Q^1 and thus does not present -Q^2-Q^2- connectivity. The latter can be observed only in an octamer Q^1-Q^2-Q^{2L}-$\mathbf{Q^2}$-$\mathbf{Q^2}$-Q^{2L}-Q^2-Q^1 or in longer chains. (Q^{2L}, the so-called bridging tetrahedral, are four-coordinate Q^2 silicate moieties that are positioned away from the interlayer space between C-S-H chains and link dimers, as shown in the inset in Fig. 4.) A series of connectivities including Q^1-Q^2, Q^2-Q^{2L} but no Q^2-Q^2 connectivities is thus a signature of pentamers. The 2D *J*-mediated $^{29}Si\{^{29}Si\}$ NMR spectrum in Fig. 4b reveals correlated intensities between the ^{29}Si SQ signal at -84.4 ppm from Q^2 species and -82.2 ppm (DQ = -166.6 ppm, *vi*), -79.7 ppm (DQ = -164.1 ppm, *vii*), and -78.2 ppm (DQ = -162.5 ppm, *viii*) that are associated with Q^{2L} species and two distinct Q^1 species, respectively. Therefore, the pairs of correlated intensities labelled *vi*, *vii*, and *viii* in the 2D spectrum (Fig. 4b) establish the presence of one Q^2-Q^{2L} and two distinct Q^2-Q^1 connectivity, respectively, in the associated C-S-H unit. Furthermore, there is no detectable correlated intensity, within the sensitivity limits of the measurement, between this Q^2 species with a ^{29}Si SQ signal at -84.4 ppm and any other resonance in the Q^2 range (only with Q^{2L} and Q^1 as stated above). This indicates that the associated C-S-H unit exhibits no direct Q^2-Q^2 connectivity, and thus, must be attributed to pentamers, as shown in the inset of Fig. 5b. This is in agreement with the previously proposed relative stabilities of C-S-H units of different chain lengths.[9,10]

Supplementary references

1. Wesselsky, A. & Jensen, O. M. Synthesis of pure Portland cement phases. *Cem. Concr. Res.* **39,** 973 – 980 (2009).

2. Skibsted, J., Hjorth, J., & Jakobsen, H. J. Correlation between ^{29}Si NMR chemical shifts and mean Si-O bond lengths for calcium silicates. *Chem. Phys. Lett.* **172,** 279–283 (1990).

3. Massiot, D. et al. Modelling one and two-dimensional solid-state NMR spectra. *Magn. Reson. Chem.* **40,** 70 – 76 (2002).

4. Skibsted, J., Hjorth, L. & Jakobsen, H. J. Quantification of thaumasite in cementitious materials by ^{29}Si $\{_1$H$\}$ cross-polarization magic-angle spinning NMR spectroscopy. *Adv. in Cem. Res*. **7,** 69-83 (1995).

5. Klur, I. Etude par RMN de la structure des silicates de calcium hydrates, PhD thesis, Université Paris VI, Paris, France (1996).

6. Klur, I. et al. NMR Cross-polarization when $T_{IS} > T_{1\rho}$; Examples from silica gel and calcium silicate hydrates. *J. Phys. Chem.* **104**, 10162-10167 (2000).

7. Grimmer, A. R., Kretschmer, A., Cajipe, V. B. Influence of Magic Angle Spinning on Sample Temperature. *Magn. Reson. Chem.* **35,** 86 - 90 (1997).

8. d'Espinose de Lacaillerie, J.-B., Jarry, B.,Pascui, O. &Reichert, D. "Cooking the sample": radiofrequency induced heating during solid-state NMR experiments. *Solid State Nucl. Magn. Reson.* **28**, 225-232 (2005).

9. Ayuela, A. et al. Silicate chain formation in the nanostructure of cement-based materials. *J. Chem. Phys.* **127,** 164710 (2007).

10. Brough, A. R., Dobson, C. M., Richardson, I. G. & Groves, G. W. In situ solid-state NMR studies of Ca_3SiO_5: hydration at room temperature and at elevated temperatures using ^{29}Si enrichment. *J. Mater. Sci.* **29,** 3926–3940 (1994).